

# Robustness Enhancement of Universal Noncyclic Geometric Gates via Evolution Optimization

Zi-Hao Qin,<sup>1</sup> Yan Liang,<sup>2,\*</sup> Yi-Han Yuan,<sup>1</sup> Zheng-Yuan Xue,<sup>1,3,†</sup> and Tao Chen<sup>1,3,‡</sup>

<sup>1</sup>Key Laboratory of Atomic and Subatomic Structure and Quantum Control (Ministry of Education),  
and School of Physics, South China Normal University, Guangzhou 510006, China

<sup>2</sup>School of Physical Science and Technology, Guangxi Normal University, Guilin 541004, China

<sup>3</sup>Guangdong Provincial Key Laboratory of Quantum Engineering and Quantum Materials,  
Guangdong-Hong Kong Joint Laboratory of Quantum Matter, and Frontier Research Institute for Physics,  
South China Normal University, Guangzhou 510006, China

(Dated: May 8, 2025)

The concept of nonadiabatic noncyclic geometric quantum computation (NNGQC) breaks the constraint of cyclic conditions and allows the system to evolve on noncyclic paths, which greatly extends the possibilities of quantum computation. By precisely controlling the evolution of quantum parameters along the noncyclic path of the Bloch sphere, NNGQC is able to realize quantum logic gates under nonadiabatic conditions, which not only improves the speed of the operation, but also increases the path degrees of freedom, providing more operational flexibility and robustness for quantum computation. However, past work on NNGQC has not given a universal solution for different gate constructions, meanwhile due to the inability to optionally avoid some trajectory segments seriously affected by systematic errors, the performance of arbitrary geometric gate is still unsatisfactory. Here we give the general scheme of NNGQC, and also summarize the optimal gate construction corresponding to different schemes, and it is worth mentioning that we creatively introduce the universal robust control. Numerical simulations verifies that it is perfectly compatible with all types of noise terms and outperforms the transmission dynamic gates and quantum logic gates in the NGQC framework in terms of gate fidelity and robustness performance. Thus, our scheme can give the ideal quantum gate construction under noncyclic conditions, which sheds light on future large-scale quantum computation.

## I. INTRODUCTION

Quantum computing utilizes quantum mechanical properties such as superposition and entanglement to perform computations [1]. Although today's quantum computers do not have the number of quantum bits required to achieve programmable large-scale computation, they still exhibit strong superiority over conventional computers. Quantum gates are the cornerstone of performing quantum computation, but it is an unavoidable fact that environmentally induced decoherence and inaccurate control of the quantum system will greatly limit the performance of quantum gates [3–6]. Because these factors cause quantum bits to lose their desired quantum mechanical properties, the states inside a quantum computer cannot be completely isolated, making decoherence inevitable.

Geometric quantum computing, as an attractive strategy for gate construction, is characterized by integrating geometric phases with inherent fault-tolerant features into the quantum control process, enabling robust geometric implementations of universal quantum gates. However, for adiabatic geometric quantum computation (GQC) [12–15], the long evolution time required to satisfy the adiabatic condition produces gates with relatively low fidelity. In contrast to earlier adiabatic quantum computation, non-adiabatic geometric quantum computation (NGQC) [20, 24–36] based on Abelian geometric phases in secondary and tertiary systems, respectively, can intrinsically prevent environmentally induced decoherence. Nevertheless, NGQC should satisfy the cyclic condition, which

causes quantum logic gates to be more sensitive to decay and dephasing errors than conventional dynamic gates. Based on this, nonadiabatic noncyclic geometric quantum computation (NNGQC) is proposed [39–42], i.e., all single quantum bit geometric gates and nontrivial double quantum bits can be realized by noncyclic nonabelian geometric phases in superconducting circuit systems. It avoids the problems associated with types of errors that do not preserve cyclicity. More importantly, NNGQC scheme breaks the restriction of the cyclic evolution condition, which not only further increases the speed of operations but also provides more path degrees of freedom.

However, there is a wide variety of NNGQC schemes available, and each of them has its own advantages and disadvantages in terms of robustness and high-fidelity gate realization for the construction of different quantum logic gates. Meanwhile, current NNGQC implementations still lack generalized robust geometric control, rendering the realized geometric gates susceptible to systematic errors and consequently leading to inevitable fidelity loss. Recently, a widely adopted approach to address the above problem is to further integrate optimal control techniques into the geometric control process. This versatile method, universally robust control [43, 44], which also mitigate the effects of unknown sources of error. Therefore, we would like to obtain a general or optimal NNGQC scheme for different gate constructions, coupled with the above control methods to realize its robustness enhancement.

Here, we complete a general classification of currently available NNGQC schemes, and based on this we propose a new evolutionary design scheme based on nonadiabatic noncyclic geometric quantum computing (NNGQC). We also propose a variety of path optimization designs with rich degrees

\* liangyan9009@163.com

† zyxue83@163.com

‡ chentamail@163.com

of freedom in conjunction with our evolutionary scheme, and select an optimal path design as a representative scheme for NNGQC. It is worth mentioning that the scheme can achieve a generalized crosstalk-resistant [45–52] geometric gate by exploiting the additional parameter degrees of freedom available during the evolution process and further path optimization. In addition, we incorporate the recently proposed generalized robustness control into the scheme architecture, thus achieving a significant enhancement in the robustness of its gate fidelity. Our scheme significantly broadens the fault tolerance of the geometric control and exhibits superior crosstalk resistance and resistance to system-generalized errors compared to conventional geometric gates and dynamic Rabi gates, regardless of the gate type. Finally, we validate the high-fidelity performance of our NNGQC scheme by utilizing a superconducting line system [58–63] and fully considering the effects of leakage error and decoherence in physically realized numerical simulations. This has implications for future theoretical and experimental studies of geometric quantum computing.

## II. NONCYCLIC GEOMETRIC EVOLUTION: A COMPREHENSIVE ANALYSIS

We begin by considering a general two-level quantum system comprising a ground state  $|0\rangle$  and an excited state  $|1\rangle$ . Arbitrary quantum control of this system can be achieved through external microwave field driving. Under the rotating wave approximation, the Hamiltonian in the interaction picture can be expressed as:

$$\mathcal{H}(t) = \frac{1}{2} \begin{pmatrix} -\Delta(t) & \Omega(t)e^{-i\phi(t)} \\ \Omega(t)e^{i\phi(t)} & \Delta(t) \end{pmatrix}, \quad (1)$$

where  $\Omega(t)$  and  $\phi(t)$  are the time-dependent driving amplitude and phase of the microwave field, respectively;  $\Delta(t)$  is the detuning with respect to the frequency difference between the microwave field and the two-level system.

To accurately describe the evolution operator associated with the aforementioned Hamiltonian, the following two orthogonal state vectors are selected for analysis:

$$|\Psi_1(t)\rangle = e^{if_1(t)} \left[ \cos \frac{\chi(t)}{2} |0\rangle + \sin \frac{\chi(t)}{2} e^{i\xi(t)} |1\rangle \right], \quad (2a)$$

$$|\Psi_2(t)\rangle = e^{if_2(t)} \left[ \sin \frac{\chi(t)}{2} e^{-i\xi(t)} |0\rangle - \cos \frac{\chi(t)}{2} |1\rangle \right], \quad (2b)$$

where  $\chi(t)$  and  $\xi(t)$  are the spherical coordinates of the state vector on the Bloch sphere as shown in Fig. 1.  $f_k(t)$  represents the overall phase accumulated, with the initial value  $f_k(0) = 0$ . The evolution detail of the state vector  $|\Psi_k(t)\rangle$  is governed by the Hamiltonian  $\mathcal{H}(t)$ , and they are connected by the Schrödinger equation  $i(\partial/\partial t)|\Psi_k(t)\rangle = \mathcal{H}(t)|\Psi_k(t)\rangle$ . [17, 18] Therefore, by characterizing the target evolution process governed by  $\chi(t)$  and  $\xi(t)$ , the Hamiltonian control parameters  $\{\Delta(t), \Omega(t), \phi(t)\}$  can be reverse engineered [19] accordingly. In this way, the correspondence between parameters can be expressed as  $\dot{\chi}(t) = \Omega(t) \sin[\phi(t) - \xi(t)]$

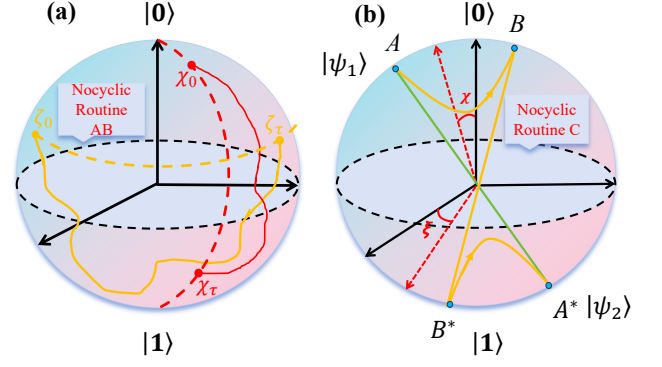


FIG. 1. (a) Implications of noncyclic geometric quantum operations. The noncyclic geometric phase is given by half of the steradian angle enclosed by the trajectory  $AB(A^*B^*)$  and the geodesic  $BA(B^*A^*)$  connecting the initial and final points. (b) Schematic representation of the possible paths satisfying the parameter settings in our three A, B, C noncyclic schemes.

and  $\dot{\xi}(t) = -\Delta(t) - \Omega(t) \cot \chi(t) \cos[\phi(t) - \xi(t)]$ . Meanwhile, we can calculate the overall phase accumulated during the evolution period as  $\gamma = f_1(\tau) - f_2(\tau) = \frac{1}{2} \int_0^\tau \frac{\dot{\xi}(t)[1 - \cos \chi(t)] + \Delta(t)}{\cos \chi(t)} dt$ . The geometric phase component in  $\gamma$  can be formally expressed as

$$\gamma_g = \gamma - \gamma_d = -\frac{1}{2} \int_0^\tau \dot{\xi}(t) [1 - \cos \chi(t)] dt, \quad (3)$$

where  $\gamma_d = -\int_0^\tau \langle \Psi_1(t) | \mathcal{H}(t) | \Psi_1(t) \rangle dt$  corresponds to the dynamical phase that is directly associated with the Hamiltonian parameters. The geometric nature of  $\gamma_g$  comes from the fact that it is given by half of the solid angle enclosed by the noncyclic evolution path and its geodesic connecting the initial point  $[\chi(0), \xi(0)]$  to the final point  $[\chi(\tau), \xi(\tau)]$ . Therefore, by ensuring that  $\gamma_d = 0$ , the evolution of this system can be a purely geometric process.

In this stage, we analyze the hierarchical relationship between geometric phases [9–11] under cyclic and noncyclic conditions. We show first how to calculate the adiabatic and nonadiabatic geometric phases. Here, we consider a Hilbert space  $\mathcal{H}$  and define  $\mathcal{H}_0 \subset \mathcal{H}$  as the set of normalized, nonzero vectors  $|\psi\rangle \in \mathcal{H}$ . A curve  $\mathcal{C}_0$  in  $\mathcal{H}_0$  is defined through vectors  $|\psi(s)\rangle$  that continuously depend on some parameter  $s \in [s_1, s_2]$ , where  $s_1, s_2$  denote the beginning and end points of the path evolution in Hilbert space, respectively. They also map the time points 0 and  $\tau$  of the evolution, which together form a four-dimensional spacetime tensor combining time and space. For a spin-1/2 particle subject to an arbitrary magnetic field  $\mathbf{B}$ , the nonadiabatic cyclic Aharonov-Anandan (AA) phase is just the solid angle determined by the evolution curve in the projective Hilbert space—a unit sphere  $S^2$ . Any two-component “spin” state  $|\psi\rangle = [e^{-i\varphi/2} \cos(\theta/2), e^{i\varphi/2} \sin(\theta/2)]^T$  may be mapped into a unit vector  $\mathbf{n} = (\sin \theta \cos \varphi, \sin \theta \sin \varphi, \cos \theta)$  in the projective Hilbert space via the relation  $\mathbf{n} = \langle \psi | \vec{\sigma} | \psi \rangle$ . By changing the magnetic field, the AA phase is given by  $\gamma = -\frac{1}{2} \int_C (1 - \cos \theta) d\varphi$ , where  $C$  is along the actual evolution

curve on  $S^2$  and is determined by the equation  $\partial_t \mathbf{n}(t) = -\mu \mathbf{B}(t) \times \mathbf{n}(t)/\hbar$ . This  $\gamma$  phase recovers Berry phase in adiabatic evolution.

Under nonadiabatic conditions,  $\gamma_g$  degenerates into the AA phase, reflecting the broader universality of geometric phases. For a Hilbert space  $\mathcal{H}$  with normalized states  $|\psi(s)\rangle \in \mathcal{H}_0 \subset \mathcal{H}$ , the total phase  $\Phi_{\text{tot}}$  transforms under gauge  $|\psi'\rangle = e^{i\alpha(s)}|\psi\rangle$  as:  $\Phi'_{\text{tot}}(\mathcal{C}_0) = \Phi_{\text{tot}}(\mathcal{C}_0) + \alpha(s_2) - \alpha(s_1)$ . The geometric phase is constructed to be gauge-invariant:

$$\Phi_g(\mathcal{C}_0) = \arg\langle\psi(s_1)|\psi(s_2)\rangle - \text{Im} \int_{s_1}^{s_2} \langle\psi(s)|\dot{\psi}(s)\rangle ds \quad (4)$$

For closed paths  $\mathcal{R}(T) = \mathcal{R}(0)$ ,  $|\psi(T)\rangle = e^{-i\Phi_{\text{dyn}}(T)} e^{i\gamma} |\psi(0)\rangle$ , where  $\gamma$  depends solely on the path's curvature (e.g., magnetic monopole in parameter space). When  $\mathcal{R}(T) \neq \mathcal{R}(0)$ , the phase combines geometric and dynamical contributions:  $|\psi(T)\rangle = \sum_k c_k(T) |k; R(T)\rangle$ ,  $\gamma = i \int_0^T \langle\psi(t)|\frac{d}{dt}\psi(t)\rangle dt$ . At the same time the total phase under the auxiliary state basis vectors becomes of the form  $\gamma_{\text{tot}}(\tau) = \text{Arg}\langle\psi(0)|e^{i\gamma(\tau)}|\psi(\tau)\rangle = \gamma(\tau) + \text{Arg}\langle\psi(0)|\psi(\tau)\rangle$  [21–23]. Removing the dynamical phase from the total phase, the remaining is the Pancharatnam geometric phase  $\gamma_g(\tau)$

$$\begin{aligned} \gamma_g(\tau) &= \gamma_{\text{tot}}(\tau) - \gamma_d(\tau) \\ &= \gamma(\tau) - \gamma_d(\tau) + \text{Arg}\langle\psi(0)|\psi(\tau)\rangle \\ &= i \int_0^\tau \langle\psi(t)|\frac{\partial}{\partial t}|\psi(t)\rangle dt + \text{Arg}\langle\psi(0)|\psi(\tau)\rangle, \end{aligned} \quad (5)$$

which is gauge invariant. This represents the general expression for the geometric phase under noncyclic conditions. Notably, when the cyclic condition  $|\psi(0)\rangle = |\psi(\tau)\rangle$  is satisfied, the argument term  $\text{Arg}\langle\psi(0)|\psi(\tau)\rangle$  vanishes, and it reduces to the conventional cyclic Aharonov–Anandan phase [3–6]. Therefore, the phase accumulated through noncyclic path is a generalization of the cyclic case.

In addition, if we regard the space of normalized states as a fiber bundle over the space of rays (a ray is defined as an equivalence class of states differing only in phase), then this bundle has a natural connection. This tells us that only if the dynamical phase is removed, the evolution of the system determined by the Schrödinger equation is based on the parallel transmission of the phases of this naturally connected system, and the Berry phase is the result of this connected curvature.

The utilization of noncyclic geometric phases allows the final system evolution to selectively fulfill one of three noncyclic evolution conditions:

- (i)  $\chi(\tau) \neq \chi(0)$  and  $\xi(\tau) = \xi(0) \pm 2n\pi$ , (6)
- (ii)  $\chi(\tau) = \chi(0)$  and  $\xi(\tau) \neq \xi(0) \pm 2n\pi$ , (7)
- (iii)  $\chi(\tau) \neq \chi(0)$  and  $\xi(\tau) \neq \xi(0) \pm 2n\pi$ . (8)

where  $n$  denotes the total number of rotations corresponding to the system's evolution along the latitude lines.

Finally, by ensuring the purely geometric nature of the evolution process through the requirement that the dynamical phase  $\gamma_d$  vanishes, we derive the parameter setting relationship during the evolution. Consequently, the corresponding

evolution operator can be expressed as

$$U(\tau) = \begin{bmatrix} e^{-i\xi_-} (iY_{\gamma',\chi_-} + Z_{\gamma',\chi_-}) & e^{-i\xi_+} (iY_{\gamma',\chi_+} - Z_{\gamma',\chi_-}) \\ e^{-i\xi_+} (iY_{\gamma',\chi_+} + Z_{\gamma',\chi_-}) & e^{-i\xi_-} (Z_{\gamma',\chi_-} - iY_{\gamma',\chi_+}) \end{bmatrix}, \quad (9)$$

where  $Y_{a,b} = \cos a \sin b$ ,  $Z_{a,b} = \cos a \cos b$ ,  $\xi_{\pm} = \frac{\xi(\tau) \pm \xi(0)}{2}$ ,  $\chi_{\pm} = \frac{\chi(\tau) \pm \chi(0)}{2}$ ,  $\gamma' = \gamma + \frac{1}{2} \int_0^\tau \dot{\gamma}(t) dt$ . Finally, we establish that the boundary values of  $\chi(t)$  and  $\xi(t)$  to realize different rotation operations.

### III. DESIGN FRAMEWORK FOR UNIVERSAL NONCYCLIC GEOMETRIC GATES

#### A. Noncyclic Geometric Evolution A

We choose (A) from the previous general model as the noncyclic condition, which is expressed in terms of polar and azimuthal angles. This condition must satisfy  $\chi(\tau) \neq \chi(0)$  and  $\xi(\tau) = \xi(0) \pm 2n\pi$ . For different values of  $n$ , it can be subdivided into two cases as follows (A<sub>1</sub>)  $\xi(\tau) = \xi(0)$ ,  $n = 0$ , (A<sub>2</sub>)  $\xi(\tau) = \xi(0) \pm 2n\pi$ ,  $n \neq 0$ . In addition, we require that all paths evolve strictly along the latitude and longitude lines of the Bloch sphere. That is, for the noncyclic conditions of class (A), it is necessary to ensure that the end point and the start point lie on the same meridian. Based on the general framework described in the previous section, we can calculate the general gate operator under the noncyclic evolution condition (A) as follows [37]:

$$U(\tau) = \begin{bmatrix} (iY_{\gamma',\chi_-} + Z_{\gamma',\chi_-}) & e^{-i\xi_+} (iY_{\gamma',\chi_+} - Z_{\gamma',\chi_-}) \\ e^{-i\xi_+} (iY_{\gamma',\chi_+} + Z_{\gamma',\chi_-}) & (Z_{\gamma',\chi_-} - iY_{\gamma',\chi_+}) \end{bmatrix} \quad (10)$$

Obviously we can build generalized quantum logic gates by setting the gate parameters: by  $\gamma' = \frac{1}{2}\pi$ ,  $\chi(\tau) + \chi(0) = \frac{1}{2}\pi$ , we can construct Hadamard gate  $H^g$ . Similarly, setting  $\gamma' = \pi$ ,  $\chi(\tau) - \chi(0) = \theta$  can construct universal  $R_{x,y}(\theta)$  gate, where  $\gamma' = \gamma + \frac{1}{2} \int_0^\tau \dot{\gamma}(t) dt$  is related to the geometric phase. Next, we will discuss the general framework for each of the two subcases under the noncyclic condition (A).

For case (A<sub>1</sub>), it is only necessary to ensure that the start and end points lie on the same meridian, without considering the specific evolution in between. However, for (A<sub>2</sub>), we require that while the start and end points are on the same longitude, the end point can perform any number of single-loop rotations in its latitudinal plane. Based on the above physical process, we provide the gate parameter settings for the two subcases.

$$\begin{aligned} \gamma'_{A_1} &= \frac{1}{2}(\xi_1 - \xi_0) \cos \chi_1 + \frac{1}{2}(\xi_2 - \xi_1) \cos \chi_2 + \cdots + \\ &\quad \frac{1}{2}(\xi_j - \xi_{j-1}) \cos \chi_j = \frac{1}{2} \sum_{i=1}^j (\xi_i - \xi_{i-1}) \cos \chi_i \\ \gamma'_{A_2} &= n_1 \pi \cos \chi_1 + \cdots + n_j \pi \cos \chi_j = \pi \sum_{i=1}^j n_i \cos \chi_i \end{aligned} \quad (11)$$

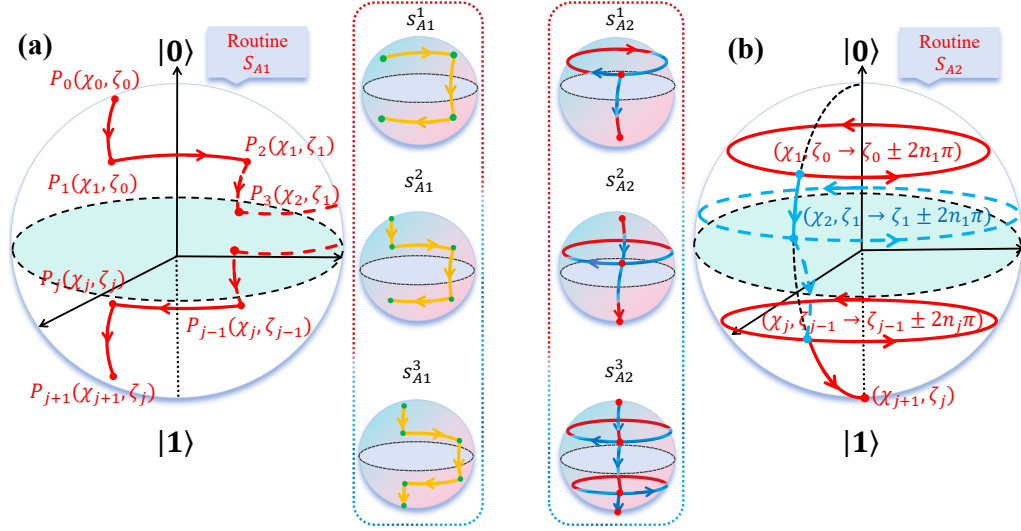


FIG. 2. (a) The first noncyclic trajectory under the noncyclic permutation condition  $A$ , which evolving along the lines of latitude and longitude through an intermediate multi-segment process. Finally returning to the same segment of longitude as the starting point. We design  $S_{A1}^{1,2,3}$  three optimization schemes based on this. (b) A possible second type of evolutionary design based on the condition of noncyclic  $A$ , i.e., coupling by latitude and longitude line evolution and a single-loop evolution structure parallel to the equatorial plane. We specifically designed  $S_{A2}^{1,2,3}$  evolution trajectory.

It is worth noting for  $(A_1)$ , there are two types of optimization parameters that can be obtained by adjusting the gate parameters:  $\{(\xi_1 - \xi_0), (\xi_2 - \xi_1), \dots, (\xi_j - \xi_{j-1})\}$ ,  $\{\chi_1, \chi_2, \dots, \chi_j\}$ . These parameters exhibit a high degree of freedom, which significantly enriching our optimization scheme. For  $(A_2)$  we also obtain two types of optimization parameters:  $\{n_1, n_2, \dots, n_j\}$ ,  $\{\chi_1, \chi_2, \dots, \chi_j\}$ . Although the range of values for the degrees of freedom in  $(A_2)$  is not as extensive as in  $(A_1)$ , these parameters can still introduce unexpected and valuable effects to our work.

### B. Improved noncyclic geometric evolution path A

Here, we first present the work related to the  $(A_1)$  subcase, where we provide possible path design diagrams. In this subcase, all path designs can be viewed as consisting of a concave-convex structure that opens to both ends. Unfortunately, the first two more conventional path designs, as shown in the Fig. 2(a), suffer from a number of limitations: due to the unitary nature of the self-generated path design, the number of path segments is insufficient, resulting in significant constraints on the range of optimizable parameters. Although fewer path segments may reduce the pulse area, our numerical simulations indicate that the robustness of the two path designs,  $S_{A1}^1, S_{A1}^2$  remains suboptimal. Most importantly, based on the requirements of the class  $(A)$  noncyclic condition, the starting and ending points of the evolution must lie on the same meridian. This imposes the condition  $\xi(\tau) - \xi(0) = \pi$  when constructing a universal  $R_{x,y}(\pi)$  gate. Consequently, the final path segment evolving along the latitudinal line collapses into a singularity, distorting the physical process and preventing the construction of a universal  $R_{x,y}(\pi)$  an outcome

we clearly wish to avoid. Fortunately, our optimized path  $S_{A1}^3$  successfully solves these issues.

We designed a ladder-like five-segment  $S_{A1}^3$  path evolution, which significantly enhances the freedom of optimization parameters. For instance, in the middle two segments of latitudinal evolution, the path parameter  $\chi$  only needs to satisfy  $\chi_1, \chi_2 \in [0, \pi]$ , thereby greatly improving the flexibility of the optimization and also cleverly resolves the issue of previous paths being unable to construct  $R_{x,y}(\pi)$ . Furthermore, numerical simulations demonstrate that this scheme also achieves higher robustness and gate fidelity. According to the evolution details of the 5-segment trajectory we can get the specific settings of the control parameters through the known parameter correspondences. For example, in the first time period  $t \in [0, \tau_1]$ , the trajectory evolves along the meridian from the initial point  $\mathbf{P}_0(\chi_0, \xi_0)$  to the point  $\mathbf{P}_1(\chi_1, \xi_1)$ . The corresponding evolution parameters satisfy  $\dot{\xi}(t) = 0$  and  $\xi(t) = \xi_0 = \xi_1$ , leading to a simplified parameter correspondence:  $\chi_1 - \chi_0 = \int_0^{\tau_1} \Omega(t) \sin[\phi(t) - \xi_0] dt$ ,  $\Delta(t) = -\Omega(t) \cot \chi(t) \cos[\phi(t) - \xi_0]$ .

Next, in order to make practical sense of our physical process, we set  $\phi(t) - \xi_0 = -\pi/2$  in the case of  $\chi_0 > \chi_1$  to ensure that the impulse area  $\int_0^{\tau_1} \Omega(t) dt$  is constantly positive and remains minimum. Meanwhile, it is not difficult to observe that the first, third, and fifth segments all evolve along the meridian. Therefore, the parameter settings of their evolution conditions can be derived in the same way, and we will not repeat them here. For the second and fourth segments, which evolve along the latitudinal line, we take the second segment as an example to elaborate. In the second time segment  $t \in [\tau_1, \tau_2]$ , there will be a starting point  $\mathbf{P}_1(\chi_1, \xi_1)$  along the latitudinal line evolution to the end point  $\mathbf{P}_2(\chi_2, \xi_2)$ . As a result, the polar angle  $\chi(t)$  and azimuthal angle  $\xi(t)$  sat-



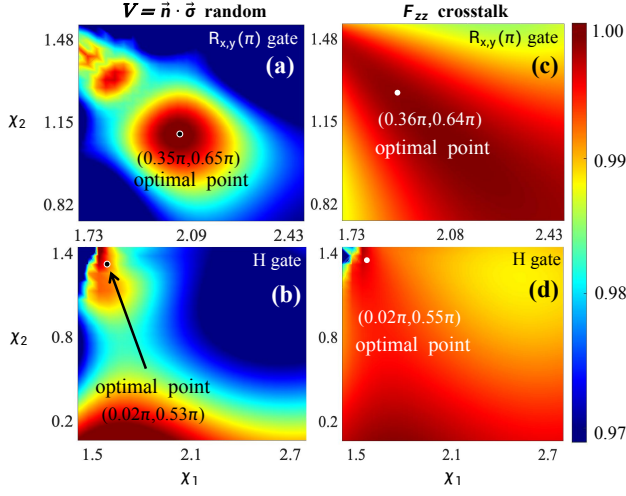


FIG. 3. (a)(b) Parameter optimization based on  $S_{A1}^3$  evolution paths. The universal error coefficient  $\lambda = 0.05$  and . By changing the values of the parameters  $\chi_1, \chi_2$ , the heat map of the gate fidelity variation with  $\chi_1, \chi_2$  is plotted, and then a set of optimal  $\chi_1, \chi_2$  values is found. (c)(d) Parameter optimization based on  $S_{A1}^3$  evolution paths under the introduction of nearest neighbor qubit ZZ crosstalk. Similarly to the above, setting  $F_{zz} = 0.05$ .

isfy  $\dot{\chi}(t) = 0$  and  $\chi(t) = \chi_1 = \chi_2$ . This leads to the following parameter constraints:  $\phi(t) = \pi + \xi(t)$ ,  $\dot{\xi}(t) = -\Delta(t) + \Omega(t) \cot \chi_1$ ,  $\phi(t) = \xi(t)$ ,  $\dot{\xi}(t) = -\Delta(t) - \Omega(t) \cot \chi_1$ .

Finally we give here all parameter setting relations for the five-segment geometric trajectory corresponding to the Hamiltonian quantity

$$t \in [0, \tau_1] : \int_0^{\tau_1} \Omega(t) dt = \chi_1 - \chi_0, \quad \phi(t) = \xi_0 + \frac{\pi}{2}, \quad (12a)$$

$$t \in [\tau_1, \tau_2] : \int_{\tau_1}^{\tau_2} \Omega(t) dt = (\xi_1 - \xi_0) \sin \chi_1 \cos \chi_1, \quad (12b)$$

$$\phi(t) = \xi_0 + \pi + \frac{\int \Omega(t) dt}{\sin \chi_1 \cos \chi_1},$$

$$t \in [\tau_2, \tau_3] : \int_{\tau_2}^{\tau_3} \Omega(t) dt = \chi_2 - \chi_1, \quad \phi(t) = \xi_2 + \frac{\pi}{2}, \quad (12c)$$

$$t \in [\tau_3, \tau_4] : \int_{\tau_3}^{\tau_4} \Omega(t) dt = (\xi_0 - \xi_1) \sin \chi_2 \cos \chi_2, \quad (12d)$$

$$\phi(t) = \xi_1 + \pi + \frac{\int \Omega(t) dt}{\sin \chi_2 \cos \chi_2},$$

$$t \in [\tau_4, \tau] : \int_{\tau_4}^{\tau} \Omega(t) dt = \chi_3 - \chi_2, \quad \phi(t) = \xi_0 + \frac{\pi}{2}, \quad (12e)$$

where the detuning values for any time segment are  $\Delta(t) = 0, -\Omega(t) \tan \chi_1, 0, -\Omega(t) \tan \chi_2$  and  $0$ , respectively.

Next, let us turn to the path design and optimization of the subcase ( $A_2$ ). Similar to the first case, we begin by designing a primitive path fragment, as illustrated in Fig. 2 (b). Initially, we expect the path design of  $S_{A2}^3$  to lead to more degrees of freedom and improved gate robustness. However, the final numerical simulation results show that this scheme not only increases the evolution time significantly, but also improves

the gate robustness and fidelity even lower than  $S_{A1}^3$ , so we choose  $S_{A1}^3$  as the representative path design of Scheme A. Please refer to Appendix A for the detailed construction of  $S_{A2}$  scheme and the comparison of the robustness tests of the  $S_{A1}^3$  and  $S_{A2}^3$  schemes.

For the  $S_{A1}^3$  pathway we first visualize the thermal and 3D distribution maps of  $\chi_1, \chi_2$  by numerical simulation in Fig. 3 (setting the error coefficients  $\lambda = 0.05$ ). Then we select the optimal combination of solutions that satisfy the highest fidelity of the constructed quantum gates, and finally change the error coefficients to achieve the simulation of the gate fidelity under URC. Similarly for  $S_{A2}^2$  and  $S_{A2}^3$  paths, the above method is repeated. The optimal parameter settings are selected through continuous optimization of  $n(S_{A2}^2)$ ,  $n_1, n_2(S_{A2}^2)$ , and finally high-fidelity gate numerical simulation is achieved. It is worth noting that  $S_{A1}^3$  is also better than  $S_{A2}^2$ , i.e., although the  $n_1, n_2$  optimization is less effective and suffers from the problem of decoherence caused by too much time, it still shows some superiority over the previous schemes.

### C. Noncyclic Geometric Evolution B

We select option (B) from the previous general model as the noncyclic condition [38], which is expressed in terms of polar and azimuthal angles. This condition satisfy  $\chi(\tau) = \chi(0)$  and  $\xi(\tau) \neq \xi(0) \pm 2n\pi$ , ensuring that the start and end points lie on the same latitude line. Based on the general model outlined in the preceding section, we can derive the gate operator under this specific condition

$$U(\tau) = \begin{pmatrix} e^{-i\xi_-} [C_{\gamma'} + iS_{\gamma'}C_\chi] & e^{-i\xi_+} iS_{\gamma'}C_\chi \\ e^{-i\xi_+} iS_{\gamma'}S_\chi & e^{-i\xi_-} [C_{\gamma'} - iS_{\gamma'}C_\chi] \end{pmatrix}, \quad (13)$$

where  $C_a = \cos a$ ,  $S_b = \sin b$ .

The subsequent configuration of the gate parameters is achieved through the utilization of the parameter setting relations inherent to the evolution process. Given the purely geometric nature of the evolution process, it is necessary to completely eliminate the dynamical phase. However, it is sufficient to satisfy  $\chi(\tau) = \chi(0) = \chi$  at the final moment, consequently, the instantaneous polar angles  $\xi(t)$  of the evolution do not need to be equal from time to time, which greatly increased the freedom in path design and evolution. Under the constraints of purely geometric conditions, we derive the following parameter-setting relations, along with the parameters of the gate operator and the designed gate operator  $\gamma' = \frac{1}{2} \int_0^t \dot{\xi}(t) \cos \chi(t) dt$ ,  $\Delta(t) = -\dot{\xi}(t) \sin^2 \chi(t)$ ,  $\gamma_g = \gamma - \gamma_d = \frac{1}{2} \int_0^t \dot{\chi}(t) [1 - \cos \chi(t)] dt$ . Based on the evolution operator obtained in the previous section, the construction of the gate parameters can be carried out by means of the parameterization relation of the evolution process. Next we try to construct the basic quantum logic gate by setting two types of parameters  $\xi(\tau), \chi(\tau)$ .

First we try to set  $\chi(\tau) = \chi_1 = 1/2\pi$  to construct single-qubit gates. However, the noncyclic geometric evolution (B) requires that  $\xi(\tau) \neq \xi(0) \pm 2n\pi$  so the  $R_{x,y}$  gate cannot

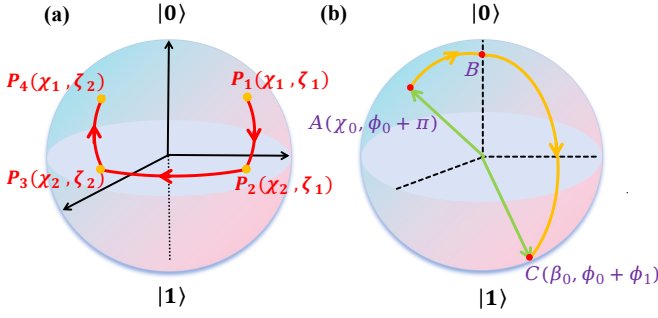


FIG. 4. (a) The optimized path under the noncyclic condition A is shaped as a 'U-shaped' path evolution with the initial and end points on the same latitude line. (b) The evolution path of state  $|\Psi_1\rangle$ , along the noncyclic path A-B-C, which starts from a given point A, and evolves along the geodesic line up to the North pole B.

be constructed in this case. Fortunately, When the following parameter settings are met by selecting a special path  $\gamma' = (\xi_2 - \xi_1) \cos \chi_2 / 2 = 1/4\pi$ ,  $\xi_2 - \xi_1 = (2n+1)\pi$  we can successfully construct the standard Hadamard gate  $H^g$  with  $\chi(\tau) = \pi/2$  when  $\xi_1 = \pi/2$ . Next, We set  $\chi(\tau) = \chi_2 = \pi$  and the same procedure as above yields the reduced gate evolution operator. Again, due to the restriction of the nocylic evolution condition of (B), we cannot construct the standard  $R_z$  rotating gate.

In summary, if the gate is constructed only by changing the parameter settings of  $\chi$ , the evolutionary process automatically falls back to cyclic conditional evolution. Obviously, it requires the path settings strictly satisfy the cyclic condition, which is clearly contrary to the nocylic condition that we are asking for. Therefore, although it is possible to construct the H gate  $H^g$  by adjusting the parameter  $\chi$  under specific conditions, the inability to construct the  $R_{x,y}$ ,  $R_z$  gates significantly diminishes the necessity of proceeding with this approach.

Second, we consider another type of parameter setting, i.e., attempting to construct standard revolving gates by setting  $\gamma'$ . we set  $\gamma' \neq \pi/2$  to obtain the evolution operator for the changed parameter setting. Subject to the condition of nocylic evolution of (B), we retain the choice of  $\xi(\tau) - \xi(0) = (2n+1)\pi$  while adding the geometric constraints  $\gamma' = \frac{1}{2} \int_0^t \dot{\xi}(t) \cos \chi(t) dt$ . This leads to the following parameter setting relation  $\cos \chi = 2\pi / (\xi(\tau) - \xi(0)) = 1/(2n+1)$ , where  $n$  is an integer. The selection of parameter values for  $n$  for different types of doors is shown in the Appendix B.

Next, by setting  $\gamma' \neq \pi$  and following the same procedure as above, we can still pick the nocylic condition of (B) while satisfying the  $\xi(\tau) - \xi(0) = \theta_Z + 2\pi$ ,  $\cos \chi = 2\pi / (\xi(\tau) - \xi(0)) = 2\pi / (\theta_Z + 2\pi)$ . With this, the universal  $R_z$  rotating gate is successfully constructed. At the same time, it is not difficult to see that  $\chi$  is an irrelevant variable of the  $R_z$  gate parameter at this time. In summary, we have successfully constructed the standard  $R_{x,y,z}$  and Hadamard gate  $H^g$  under the type of nocylic (B) evolution conditions.

#### D. Improved noncyclic geometric evolution path B

Based on the above general geometric framework in (B), we can set time-dependent shapes of parameters  $[\xi(\tau), \chi(\tau)]$  to realize different geometric evolution processes. We here design a geometric scheme based on a evolution path as Fig. 4 (a), with state parameters  $[\xi(\tau), \chi(\tau)]$  as

$$\chi(0) = \chi_1 \rightsquigarrow \chi(\tau_1) = \chi_2 \rightarrow \chi(\tau_2) = \chi_2 \rightarrow \chi(\tau) = \chi_1, \quad (14)$$

$$\xi(0) = \xi_1 \rightarrow \xi(\tau_1) = \xi_1 \rightsquigarrow \xi(\tau_2) = \xi_2 \rightarrow \xi(\tau) = \xi_2, \quad (15)$$

where the arrows  $\rightsquigarrow$  and  $\rightarrow$  indicate whether the parameters  $[\xi(\tau), \chi(\tau)]$  remain constant or change with time during the evolution process, respectively. For example, in the first time segment  $t \in [0, \tau_1]$ , the trajectory evolves from initial point  $\mathbf{P}_1(\chi_1, \xi_1)$  to point  $\mathbf{P}_2(\chi_2, \xi_1)$  along the longitude line, where the corresponding evolution parameter satisfies  $\dot{\xi}(t) = 0$  and  $\xi(t) = \xi_1 = \xi_2$ . The constraints for the dressed-state parameters reduce to  $\chi_1 - \chi_0 = \int_0^{\tau_1} \Omega(t) \sin[\phi(t) - \xi_0] dt$ ,  $\Delta(t) = -\Omega(t) \cot \chi(t) \cos[\phi(t) - \xi_0]$ . Thus, we further choose  $\phi(t) - \xi_0 = -\pi/2$  while  $\chi_1 > \chi_2$  to ensure that the pulse area  $\int_0^{\tau_1} \Omega(t) dt$  is positive and minimal.

The visualized state evolution on a Bloch sphere starts from point  $\mathbf{P}_1(\chi_1, \xi_1)$  and evolve along the longitude line with  $\chi(\tau) = \chi_1$  to point  $\mathbf{P}_2(\chi_2, \xi_1)$  at  $t \in [0, \tau_1]$ . Then it evolves along the latitude line with  $\xi(t) = \xi_2$  to point  $\mathbf{P}_3(\chi_2, \xi_2)$  at time  $t \in [\tau_1, \tau_2]$ . Finally, evolve to point  $\mathbf{P}_4(\chi_1, \xi_2)$  along the longitude line with  $\chi(\tau) = \chi_2$  at the final time  $t \in [\tau_2, \tau]$ . Therefore, under the above evolution process, according to the parameter limited relations, we can determine all the Hamiltonian parameters  $\Omega(t)$  and  $\phi(t)$  in the three segments  $t \in [0, \tau_1]$ ,  $t \in [\tau_1, \tau_2]$  and  $t \in [\tau_2, \tau]$ , where the detuning values for any time segment are  $\Delta(t) = 0$ ,  $\frac{-(\xi_2 - \xi_1) \sin^2 \chi_2}{\tau_2 - \tau_1}$ , 0.

$$t \in [0, \tau_1] : \int_0^{\tau_1} \Omega(t) dt = \chi_1 - \chi_0, \quad \phi(t) = \xi_0 - \frac{\pi}{2} \quad (16a)$$

$$t \in [\tau_1, \tau_2] : \int_{\tau_1}^{\tau_2} \Omega(t) dt = (\xi_2 - \xi_1) \cos \chi_2 \sin \chi_2 \quad (16b)$$

$$\phi(t) = \xi_1 + \pi \int_{\tau_1}^{t'} \Delta(t') dt' + \cot \chi_2 \int_{\tau_1}^{t'} \Omega(t') dt'$$

$$t \in [\tau_2, \tau_3] : \int_{\tau_2}^{\tau_3} \Omega(t) dt = \chi_1 - \chi_0, \quad \phi(t) = \xi_1 - \frac{\pi}{2}. \quad (16c)$$

#### E. Noncyclic Geometric Evolution C

Finally, we focus on introducing how to design the noncyclic geometric gate using the piecewise continuous Hamiltonian in scheme (C) [39, 40]. As shown in Fig. 4 (b), the entire evolution path of the quantum gate is divided into two distinct segments, labeled as paths AB and BC. In the first segment of the evolution,  $|\Psi_1\rangle$  starts from a given point A and evolves along the geodesic line to the North pole B. Subsequently, in the second segment, it descends to a given point C

along another geodesic line. Using this dressed states basis, the evolution operator  $U_n(\chi_0, \phi_0, \phi_1, \beta_0)$  can be expressed as  $U_n = e^{i\gamma}|\Psi_1(T_C)\rangle\langle\Psi_1(T_A)| + e^{-i\gamma}|\Psi_2(T_C)\rangle\langle\Psi_2(T_A)|$ , where  $\gamma$  is the associated phase that is obtained. This two-segment path in the dressed state basis is not closed. The quantum gate using here is two-pieces of Hamiltonian in Equ. 1, for each segment the Hamiltonian can be written in the following form

$$H_n(t) = \begin{cases} \frac{\Omega_0}{2} (\cos(\phi_0 + \frac{\pi}{2})\sigma_x + \sin(\phi_0 + \frac{\pi}{2})\sigma_y), & T_A \leq t < T_B \\ \frac{\Omega_0}{2} (\cos(\phi_0 + \phi_1 + \frac{\pi}{2})\sigma_x + \sin(\phi_0 + \phi_1 + \frac{\pi}{2})\sigma_y), & T_B < t \leq T_C \end{cases} \quad (17)$$

where  $T_B - T_A = \chi_0/\Omega_0$  and  $T_C - T_B = \beta_0/\Omega_0$ . These are then connected together at the last moment to form a desired quantum gate as Eq. (18).

Here, the parameters  $\chi_0$ ,  $\phi_0$ ,  $\phi_1$ , and  $\beta_0$  are determined by the selected evolution operator. Notably, the operator  $U_n(\chi_0, \phi_0, \phi_1, \beta_0)$  is capable of facilitating arbitrary rotations on the Bloch sphere. For instance,  $U_n(x_0, \frac{\pi}{2}, \pi, \beta_0)$  and  $U_n(x_0, -\pi, \pi, \beta_0)$  can be used to implement rotations around the  $x$ -axis and  $y$ -axis, respectively. The rotation angle for both cases is given by  $\beta_0 - \chi_0$ . It is important to note that, while there are multiple choices for  $\chi_0$  and  $\beta_0$  when designing rotations around the  $x$ -axis or  $y$ -axis, the conditions  $\chi_0 > 0$  and  $\beta_0 > 0$  must be satisfied. These constraints ensure that the evolution time remains positive and prevent the gate from degenerating into a trivial pulse sequence.

$$U_n(\chi_0, \phi_0, \phi_1, \beta_0) = U_{CB}(T_C, T_B)U_{BA}(T_B, T_A) \quad (18)$$

$$= \begin{pmatrix} \cos \frac{\chi_0}{2} \cos \frac{\beta_0}{2} - \sin \frac{\chi_0}{2} \sin \frac{\beta_0}{2} e^{-i\phi_1} & -\cos \frac{\chi_0}{2} \sin \frac{\beta_0}{2} e^{-i(\phi_0+\phi_1)} - \cos \frac{\beta_0}{2} \sin \frac{\chi_0}{2} e^{-i\phi_0} \\ \cos \frac{\chi_0}{2} \sin \frac{\beta_0}{2} e^{i(\phi_0+\phi_1)} + \cos \frac{\beta_0}{2} \sin \frac{\chi_0}{2} e^{i\phi_0} & \cos \frac{\chi_0}{2} \cos \frac{\beta_0}{2} - \sin \frac{\chi_0}{2} \sin \frac{\beta_0}{2} e^{i\phi_1} \end{pmatrix}$$

#### IV. GATE ERROR ROBUSTNESS

##### A. Universal Robust Control

Before proceeding to the numerical simulations, we would like to highlight a unique Universal Robust Control (URC) [43, 44] framework introduced in our work. This framework provides a straightforward cost function that can be minimized to ensure universal robustness in quantum control problems, representing a significant innovation in our approach. Our construction is based on a superoperator formalism, where the operator  $\mathcal{M}_0[V] \equiv \tilde{V}_0$  can be interpreted as the action of a linear superoperator  $M_0$  acting on  $V$ , under the assumption that  $\text{Tr}V=0$ . However, since the trace of any operator  $V$  is unitarily invariant, for the identity operator  $I$ , we have  $M_0|I\rangle = |I\rangle$ , meaning the norm of  $M_0$  cannot be arbitrarily reduced. To address this issue, we restrict our analysis to the set of traceless perturbation operators by defining a projector in the doubled Hilbert space:  $P_0 = |I\rangle\langle I|/d$  such that  $P_0|A\rangle = \text{Tr}(A)|I\rangle/d$ . We then redefine the relevant superoperator as:

$$\tilde{M}_0 = M_0(I - P_0). \quad (19)$$

For any operator  $V'$ , this acts as

$$\tilde{M}_0|V'\rangle = M_0(I - P_0)|V'\rangle = M_0|V\rangle = |\tilde{V}_0\rangle, \quad (20)$$

where  $V$  is a traceless version of  $V'$ . The URC framework demonstrates that for general quantum systems, the connec-

tion between robustness and various error correction methods can be translated into a requirement for a single object—the superoperator  $\tilde{M}_0$  to be robust to first-order perturbations. This allows us to formulate a quantum optimal control problem to find evolutions that achieve a predefined target while remaining robust to arbitrary perturbations.

In our work, Gate fidelity was a function of perturbation strength  $\lambda$  for the cases where the  $V = \vec{n} \cdot \vec{\sigma}$  with  $\vec{n}$  a random unit vector, which is defined in the following form

$$URC = \begin{pmatrix} \lambda\Omega_m C_\theta & \lambda\Omega_m (S_\theta C_\varphi - iS_\theta S_\varphi) \\ \lambda\Omega_m (S_\theta C_\varphi + iS_\theta S_\varphi) & \lambda\Omega_m C_\theta \end{pmatrix} \quad (21)$$

where  $S_\theta = \sin\theta$ ,  $C_\theta = \cos\theta$ ,  $S_\varphi = \sin\varphi$ ,  $C_\varphi = \cos\varphi$ . The URC scheme introduces a universal robust geometric control method based on geometric trajectory correction. This method effectively reduces sensitivity to systematic errors by introducing additional evolutionary parameters without imposing further experimental requirements. Moreover, the scheme employs a multi-segment geometric trajectory correction technique, which enhances the robustness of quantum gates by carefully designing the evolution paths of quantum states in the Hilbert space and optimizing the control parameters along these trajectories. Compared to traditional quantum errors like bit-frequency drift and bubble errors, the URC scheme addresses a wider range of systematic errors in gate operations. While conventional methods rely on precise field control, URC enhances robustness by optimizing quantum state evolution paths, ensuring high-fidelity gates.

## B. ZZ-crosstalk model

In the following section, we will enhance the crosstalk immunity characteristics of the constructed gates by optimizing parameters based on the aforementioned path evolution. To achieve this, we consider a generalized 2D lattice model for scalable quantum computing. Here, scalable quantum computing refers to the ability to efficiently apply the current scheme to large-scale quantum systems, even in the presence of residual connections, while relying solely on local control. To ensure the universality of the scheme, we assume that the lattice consists of an  $N \times N$  array of physical qubits, as illustrated in Fig. 5. Furthermore, we label the qubits located in the  $i$ -th row and  $j$ -th column as  $Q_{ij}$ . In typical solid-state quantum systems, the two independently drivable nearest-neighbor qubits are coupled via XY-type interactions, specifically, the dynamical behavior of the system is governed by the total Hamiltonian:  $H(t) = H_0(t) + H_{zz}$ , where  $H_0(t) = H_d(t) + H_J(t)$  represents the free Hamiltonian. Here  $H_d(t)$  denotes the Hamiltonian volume with a single quantum bit driving it, and  $H_J(t)$  describes the interaction between the nearest neighboring quantum bits of the system. The term  $H_{zz}$  accounts for the ZZ crosstalk effects [45–52]. In the interaction picture, the Hamiltonian for a single qubit driven at resonance is given by the following equation: ( $\hbar = 1$ ):

$$H_{zz} = \sum_{ij} (\eta_{ij}^x \sigma_{ij}^z \sigma_{i+1,j}^z + \eta_{ij}^y \sigma_{ij}^z \sigma_{i,j+1}^z) \quad (22a)$$

$$H_d(t) = \sum_{ij} \Omega_{ij}(t) (\cos \phi_{ij} \sigma_{ij}^x + \sin \phi_{ij} \sigma_{ij}^y) \quad (22b)$$

$$H_J(t) = \sum_{ij} \frac{J_{ij}^x(t)}{2} (\sigma_{ij}^x \sigma_{i+1,j}^x + \sigma_{ij}^y \sigma_{i,j+1}^y) + \sum_{ij} \frac{J_{ij}^y(t)}{2} (\sigma_{ij}^x \sigma_{i,j+1}^x + \sigma_{ij}^y \sigma_{i+1,j}^y), \{i, j\} \in \{1, 2, \dots, N\} \quad (22c)$$

where  $\Omega_{ij}(t)(\phi_{ij})$  is the time-containing pulse drive (phase) acting on Qubit  $Q_{ij}$ ,  $\eta_{ij}^{x,y}$  characterize the coupling strength of

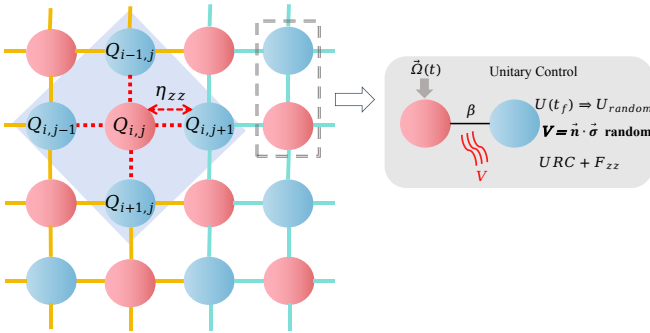


FIG. 5. Schematic illustration on a two-dimensional  $N \times N$  physical qubits lattice: in this superconducting quantum bit lattice, there is ZZ crosstalk between the target control quantum bit and its neighboring bystander quantum bit, as well as a universal control error.

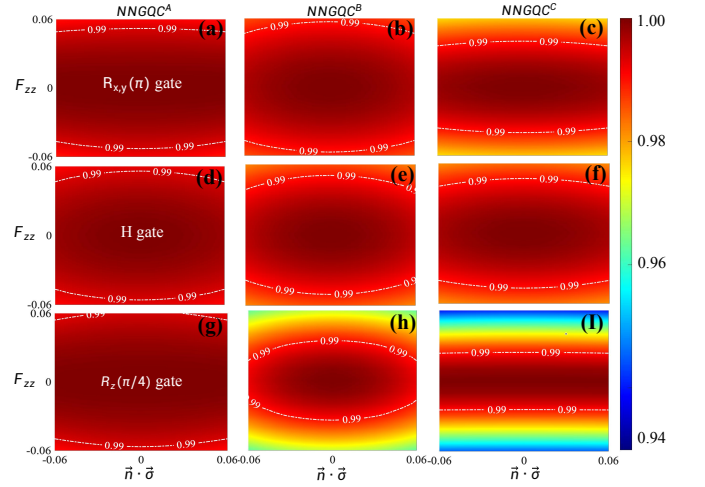


FIG. 6. Generalized gate robustness test under two different types of error controls constructed based on  $ABC$  noncyclic scheme. Numerical simulations show that different gates have their own robustness under different schemes and the combined effect of universal error and ZZ crosstalk. (a)(d)(g) is the optimal scheme for different generic gates  $R_{xy}(\pi)$ ,  $H^g$ ,  $R_z(\pi/4)$ .

ZZ interactions between nearby Qubits.  $\sigma_{ij} = (\sigma_{ij}^x, \sigma_{ij}^y, \sigma_{ij}^z)$  is the Pauli operator, and  $J_{ij}^x(t), J_{ij}^y(t)$  are the controlled coupling strengths between  $Q_{ij}$  and its nearest neighboring quantum bits along the rows and columns directions, respectively. Finally, we define the formula for calculating the error sensitivity of ZZ crosstalk as

$$F(\zeta_{zz}) = \text{Tr}(U^\dagger U_{zz}) / \text{Tr}(U^\dagger U). \quad (23)$$

It is utilized to evaluate the impact of crosstalk error  $\mathcal{H}_{zz}$  on gate fidelity, where  $U$  and  $U_{zz}$  represent the desired gate and the crosstalk-affected gate, respectively.

## C. High-fidelity gate simulation with optimized scheme

In this stage, we construct single-qubit gates under  $(ABC)$  scheme, and show the physical realization of their gate fidelity through numerical simulations. Based on the two types of errors discussed in the previous section, through numerical simulation we find that: different universal quantum gates have different sensitivities to the types of errors. Compared to the noncyclic condition  $(A, C)$ , the  $(B)$  condition allows for a simpler construction of universal  $R_z$  rotating gates, which is theoretically more generalizable. For the  $(A)$  and  $(C)$  schemes we use composite superposition for  $R_z$  gate construction.

Finally, we come to test the robustness of the  $(ABC)$  scheme for various gate types in a comprehensive manner with simultaneous compatibility of the two error types. Ultimately, we find that the single-qubit gate constructed based on different noncyclic schemes are robust in different noise-error environments, and we give the optimal single-qubit gate construction schemes in Fig. 6. Through numerical simulations, we



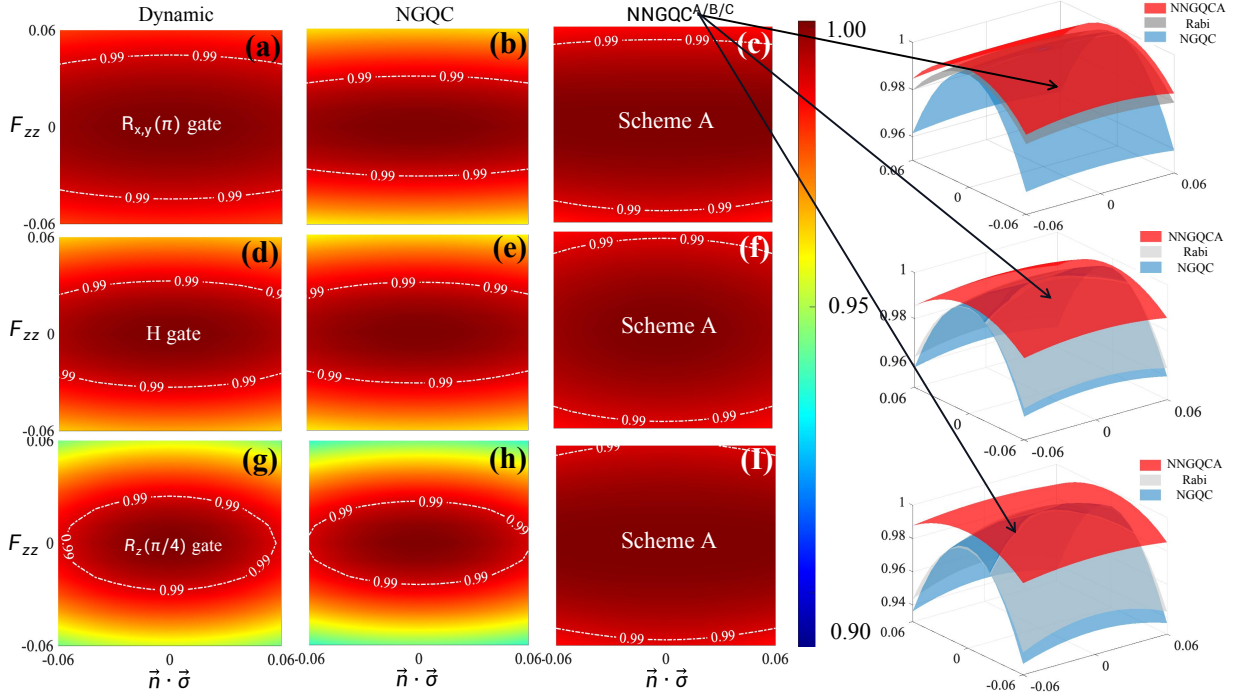


FIG. 7. Comparison of the robustness of the optimal generic quantum under  $ABC$  and the quantum gates under the conventional NGQC scheme, dynamic gates scheme. (c)(g)(i) demonstrate the superiority of the noncyclic A scheme for a set of two error ranges ( $URC \oplus F_{zz}$ ). To visualize the robustness effect, we also give a three-bit robustness comparison test under the joint error in the right column.

find that each generic quantum gate based on the noncyclic A scheme (i.e.  $S_{A1}^3$  path-optimized design), exhibits the most significant superiority compared to the B, C scheme. Based on this, we select the optimal quantum gates of each type in Fig. 6 and compare their robustness with those constructed under the traditional cyclic and [56, 57] dynamical schemes [53–55] (see Appendix C, D for details). According to the final results shown in Fig. 7, we find that the robustness is much better than the existing conventional schemes, which is useful for future work.

## V. HIGH-FIDELITY SUPERCONDUCTING IMPLEMENTATION

At this stage, we focus on the implementation of two-logical-qubit gates in superconducting circuits [58–61], which represents a crucial and nontrivial component in the construction of universal quantum gates. Our analysis begins with an examination of the energy level structure of a single transmon qubit. The energy distribution across different eigenstates  $|k\rangle$  can be described by the free Hamiltonian (specifying  $\hbar = 1$ )

$$\mathcal{H}_0 = \sum_{k=0}^{+\infty} \left[ k\omega_q - \frac{k(k-1)\alpha}{2} \right] |k\rangle\langle k|, \quad (24)$$

where  $\alpha$  is the weaker anharmonicity term and  $\omega_q$  is the bare quantum bit transition frequency. Within the Hilbert space

spanned by the tensor product of the two lowest energy eigenstates  $|0\rangle$  and  $|1\rangle$ , we introduce an external driving field to the system in the laboratory frame. Through the application of a picture transformation, we derive the corresponding driving Hamiltonian in the rotating frame, which takes the following form:

$$\begin{aligned} \mathcal{H}_{leak}(t) = & \sum_{k=0}^{+\infty} \left[ \left( k - \frac{1}{2} \right) \Delta(t) - \frac{k(k-1)\alpha_k}{2} \right] |k\rangle\langle k| \\ & + \left[ \frac{1}{2} \Omega(t) e^{-i\phi(t)} \sum_{k=0}^{+\infty} \sqrt{k+1} |k\rangle\langle k+1| + \text{H.c.} \right] \end{aligned} \quad (25)$$

It is crucial to emphasize that  $\alpha_k$ , representing the intrinsic anharmonicity of the transmon qubit, characterizes unwanted transitions from the computational subspace spanned by  $|0\rangle$ ,  $|1\rangle$  to a higher level, which significantly limits the gate fidelity. These transitions impose significant limitations on the achievable gate fidelity. Furthermore, decoherence effects arising from the inevitable coupling between the quantum system and its environment constitute another critical factor that impacts the physical implementation. In our theoretical framework, we incorporate both of these effects through the quantum dynamics described by the Lindblad master equation [64]

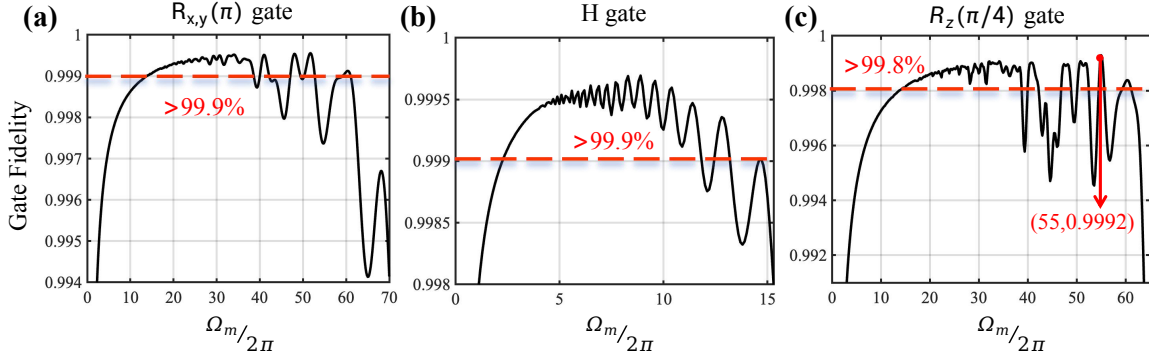


FIG. 8. Performance of single-qubit geometric gates. Gate fidelity results for (a)  $R_x(\pi)$ , (b)  $H^g$  and (c)  $R_z(\pi/4)$  geometric gates as a function of the tunable parameter  $\Omega_m$ .

$$\begin{aligned} \dot{\rho}_1 = & -i[\mathcal{H}(t) + \mathcal{H}_{\text{leak}}(t), \rho_1] \\ & + \sum_{k=1}^{+\infty} \left\{ \frac{\kappa_-^k}{2} \mathcal{D}(\sqrt{k+1}|k\rangle\langle k+1|) + \frac{\kappa_z^k}{2} \mathcal{D}(|k+1\rangle\langle k+1|) \right\}, \end{aligned} \quad (26)$$

where  $\kappa_-^l$  and  $\kappa_z^l$  denote the relaxation and dephasing rates of transmon qubit, respectively.  $\rho_1$  is the density matrix, and  $\mathcal{D}(A) = 2A\rho_1 A^\dagger - A^\dagger A\rho_1 - \rho_1 A^\dagger A$  corresponds to the Lindblad superoperator associated with operator  $A$ .

Here, we perform the quantum logic gate implementation of superconducting circuits by selecting the  $H^g$  and  $R_x(\pi)$  gates from the previous section. Starting from the defined initial state  $|\psi_1\rangle$ , the ideal final states under the action of these two geometric gates are  $|\psi_{f_H}\rangle = H^g|\psi_1\rangle$  and  $|\psi_{f_X}\rangle = X_{\pi/2}^g|\psi_1\rangle$ , respectively. Next, the value of their gate fidelity can be derived according to formula  $F_{k=H,X}^G = \frac{1}{2\pi} \int_0^{2\pi} \langle \psi_{f_k} | \rho_1 | \psi_{f_k} \rangle d\vartheta_1, \vartheta_1 \in [0, 2\pi]$  [65].

From the simulation results, we can find that, limited by the impacts of leakage error, which proportional to  $\Omega_m$  and decoherence (inversely proportional to  $\Omega_m$ ), the resulting gate fidelity cannot reach a high level. In practical physical implementations, the weak anharmonicity of transmon qubits introduces significant challenges. When a target microwave field is applied to drive transitions between the two lowest energy levels, it simultaneously induces dispersive transitions among higher excited states. These unintended sequential transitions between higher energy levels lead to leakage errors, compromising the independence of quantum bit state operations. To address this issue and enable independent qubit operations, we apply recent theoretical explorations of removing derivatives via an adiabatic gate (DRAG) [71–73] to suppress this type of leakage error (for details, see App. E).

To further analyze the performance of single-qubit geometric gates, we use the geometric operations  $H^g$  and  $R_x(\pi)$  gate as two typical examples. In our simulations, from the state-of-the-art experiment, we choose the relaxation rate and the phase-shift rate of the Transmon to be the same as  $\kappa_1 = \kappa_2 = 2\pi \times 2$  kHz, and the anharmonicity to be  $\alpha = 2\pi \times 320$  MHz. Numerical simulations (Fig. 8) reveal that, when

$\Omega_m = 2\pi \times 51$  MHz for  $R_x(\pi)$  gate,  $\Omega_m = 2\pi \times 9$  MHz for  $H^g$  gate, and  $\Omega_m = 2\pi \times 55$  MHz for  $R_z(\pi/4)$  gate. The fidelity reach 99.95%, 99.96%, and 99.92% respectively. These results demonstrate that the single-qubit gates realized via our NNGQC scheme in superconducting systems achieve fidelity comparable to the highest experimental standards.

Generally, Our proposed NNGQC scheme is particularly suitable for implementing superconducting two-qubit entanglement gates, enabling generalized fault-tolerant quantum computation when supplemented with single-qubit gates.

However, for capacitively coupled transmon quantum bits  $|T_i, T_j\rangle = |T_i\rangle_i \otimes |T_j\rangle_j$ , the coupling strength is fixed and difficult to adjust. Additionally, the frequency difference  $\Delta_i = \omega_i - \omega_j$  between two quantum bits is usually fixed and usually non-zero, meaning they generally cannot exchange energy resonantly. To ensure resonant coupling when operating at the optimal point—allowing neighboring transmons to be freely tuned—we apply an AC-driven magnetic flux to one of them (e.g.,  $T_i$ ), modulating its frequency into a periodic oscillation of the form [67–69]  $\omega_i(t) = \omega_i + \epsilon_i \sin(\nu_i t + \phi_i)$ . This modulation can effectively bring the qubit’s sideband into resonance with the cavity frequency, as becomes clear when transforming to the rotating frame defined by  $U = U_1 \times U_2$ .

$$\begin{aligned} U_1 = & \exp \left[ -i \left( \frac{\omega_q}{2} \sigma_j^z + \omega_c a^\dagger a \right) t \right] \\ U_2 = & \exp \left[ i \sigma_j^z \frac{\alpha_j}{2} \cos(\omega_j t - \varphi_j) \right], \end{aligned} \quad (27)$$

where  $\alpha_j = \epsilon_j/\omega_j$ ,  $\omega_{q,j}$  is the energy splitting of the transmon qubit and  $\sigma_j^z$  is the Pauli matrix of the  $j$  th transmon qubit in its eigenbasis. Next we use the Jacobi-Anger identity of

$$\exp[-i\beta_i \cos(\nu_i t + \phi_i)] = \sum_{n=-\infty}^{\infty} (-i)^n J_n(\beta_i) e^{-in(\nu_i t + \phi_i)}, \quad (28)$$

where  $J_n(\beta_i) = (-1)^m J_m(\beta_i)$ ,  $J_m(\beta_i)$  is Bessel functions of the first kind. The transformed Hamiltonian can be written

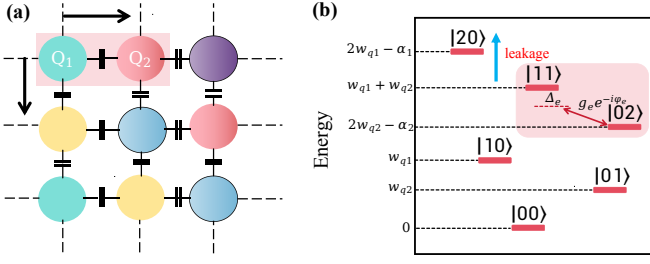


FIG. 9. (a) A scalable 2D quantum bit lattice consisting of capacitively coupled superconducting transmon (b) Energy level structure of two capacitively coupled transconjugate elements  $Q_1$  and  $Q_2$ , where  $|00\rangle, |01\rangle, |10\rangle, |11\rangle$  as the computational basis vectors open into a subspace, and the remaining high-energy levels act as leaky subspaces.

as

$$\begin{aligned} \mathcal{H}_{ij} = \sum_{n=-\infty}^{+\infty} (-i)^n J_n(\beta_i) g_{ij} \{ & |10\rangle_{ij} \langle 01| e^{i\Delta_i t} e^{-in(\nu_i t + \phi_i)} \\ & + \sqrt{2} |11\rangle_{ij} \langle 02| e^{i(\Delta_i + \alpha_j)t} e^{-in(\nu_i t + \phi_i)} \\ & + \sqrt{2} |20\rangle_{ij} \langle 11| e^{i(\Delta_i - \alpha_i)t} e^{-in(\nu_i t + \phi_i)} \} + \text{H.c.}, \end{aligned} \quad (29)$$

By neglecting the higher-order oscillatory terms of the rotating-wave approximation (RWA), we find that the resonant coupling in both the single and double-excitation subspaces can be effectively controlled by modulating the qubit frequency-driving parameters  $(\epsilon_i, \nu_i)$ . Specifically, the parametrically tunable coupling can be selectively addressed in the single-excitation subspace  $|01\rangle_{12}, |10\rangle_{12}$  and the two-excitation subspace  $|02\rangle_{12}, |11\rangle_{12}, |20\rangle_{12}$ , by adjusting the driving frequency  $\nu$  and the ratio  $\beta$ . This enables the realization of our target two-qubit geometric gates: the iSWAP gate (via single-excitation subspace coupling).

Next, in order to construct the two-qubit ensemble iSWAP gate and obtain the parameter-tunable coupling in the single-exciton space  $|01\rangle, |10\rangle$ , we adjust the drive frequency  $\nu$  to satisfy  $\Delta_i - \nu = -\Delta_t$ , where  $|\Delta_t| \ll |\nu, \Delta_i|$  is a small quantity. With this parameter settings, the perturbation term between  $|01\rangle, |10\rangle$ , as well as the leakage interaction between  $|02\rangle$  and  $|11\rangle$  go into dispersion [77–79]. Under such consideration, the energy spectrum is shown in Fig. 9 (b). Now we apply an extra unitary transformation  $\mathcal{R}_2(t) = \exp\{-i\Delta_e t(|01\rangle\langle 01| - |10\rangle\langle 10|)/2\}$ , the effective Hamiltonian similar to Eq. 1 in this frame is given by

$$\mathcal{H}_e(t) = \frac{1}{2} \begin{pmatrix} -\Delta_e & g_e e^{-i\varphi_e} \\ g_e e^{i\varphi_e} & \Delta_e \end{pmatrix}, \quad (30)$$

where  $g_e \equiv 2J_1(\beta)g_{12}$  and  $\varphi_e = (\Delta_t - \Delta_e)t + \varphi - \pi/2 = \eta t + \varphi - \pi/2$ .

In the following, to construct iSWAP gates, we choose a set of orthogonal state vectors [70] as computational basis vectors

:

$$\begin{aligned} |\Psi_1(t)\rangle &= e^{if_1(t)} \left[ \cos \frac{\chi(t)}{2} |01\rangle + \sin \frac{\chi(t)}{2} e^{i\xi(t)} |10\rangle \right], \\ |\Psi_2(t)\rangle &= e^{if_2(t)} \left[ \sin \frac{\chi(t)}{2} e^{-i\xi(t)} |01\rangle - \cos \frac{\chi(t)}{2} |10\rangle \right], \\ |\Psi_3(t)\rangle &= |00\rangle, \\ |\Psi_4(t)\rangle &= |11\rangle, \end{aligned} \quad (31)$$

Since  $|\Psi_3(t)\rangle, |\Psi_4(t)\rangle$  contains no time, which is decoupled from dynamics of the system  $H_e(t)$ . The evolution of  $|\Psi_1(t)\rangle, |\Psi_2(t)\rangle$  characterized by the parameters  $\chi(t)$  and  $\xi(t)$  can also be described on the Bloch sphere spanned by the effective two-dimensional subspace  $|01\rangle, |10\rangle$ . Based on this, the parameter settings of the two-qubit Hamiltonian  $H_e(t)$  corresponding to the five-segment geometric trajectory under the  $S_{A1}^3$  path optimization can be simplified as

$$t \in [0, \tau_1] : g_e \tau_1 = \chi_1 - \chi_0, \quad \phi_e = \xi_0 + \frac{\pi}{2}, \quad (32a)$$

$$t \in [\tau_1, \tau_2] : g_e(\tau_2 - \tau_1) = (\xi_1 - \xi_0) \sin \chi_1 \cos \chi_1, \quad \phi_e = \xi_0 + \pi + \frac{g_e t}{\sin \chi_1 \cos \chi_1}, \quad (32b)$$

$$t \in [\tau_2, \tau_3] : g_e(\tau_3 - \tau_2) = \chi_2 - \chi_1, \quad \phi_e = \xi_1 + \frac{\pi}{2}, \quad (32c)$$

$$t \in [\tau_3, \tau_4] : g_e(\tau_4 - \tau_3) = (\xi_0 - \xi_1) \sin \chi_2 \cos \chi_2, \quad \phi_e = \xi_1 + \pi + \frac{g_e t}{\sin \chi_2 \cos \chi_2}, \quad (32d)$$

$$t \in [\tau_4, \tau] : g_e(\tau - \tau_4) = \chi_3 - \chi_2, \quad \phi_e = \xi_0 + \frac{\pi}{2}. \quad (32e)$$

Similarly to the previous section, the effective detuning quantities for each segment are  $\Delta(t) = 0, -g_e \tan \chi_1, 0, -g_e \tan \chi_2$  and  $0$ , respectively. By setting the gate parameters  $\{\chi_0, \xi_0, \gamma_g\} = (0, \pi/2, \gamma_g)$ ,  $\gamma_g = (\xi_1 - \xi_0)[\cos \chi_1 - \cos \chi_3]/2$ . The final evolution operator unfolded under the computational basis vector space  $|00\rangle, |01\rangle, |10\rangle, |11\rangle$

$$\text{iSWAP}^{\text{NNGQC}} = \begin{pmatrix} 1 & 0 & 0 & 0 \\ 0 & 0 & i & 0 \\ 0 & i & 0 & 0 \\ 0 & 0 & 0 & 1 \end{pmatrix}, \quad (33)$$

In this way, we construct the iSWAP gate based on the optimization under the five-segment path fragmentation. Finally, we evaluate the gate fidelity of the two-qubit geometric gates iSWAP in the superconducting realization under our NNGQC scheme. We define the density matrix of a two-qubit system as  $\rho_2$ . Similar to the single-qubit gate case above, we use the following equation  $F_{U_2}^G = \frac{1}{4\pi^2} \int_0^{2\pi} \int_0^{2\pi} \langle \psi_{f_{U_2}} | \rho_2 | \psi_{f_{U_2}} \rangle d\vartheta_1 d\vartheta_2$  [66], where  $|\psi_{f_{U_2}}\rangle = U_2 |\psi_2\rangle$  is the ideal final state with a general initial state of two coupled qubits being  $|\psi_2\rangle = (\cos \vartheta_1 |0\rangle_1 + \sin \vartheta_1 |1\rangle_1) \otimes (\cos \vartheta_2 |0\rangle_2 + \sin \vartheta_2 |1\rangle_2)$ .

Next, in our simulation, The quantum bit parameter setting for transmon Q1 is determined as the anharmonicity  $\alpha = 2\pi \times$

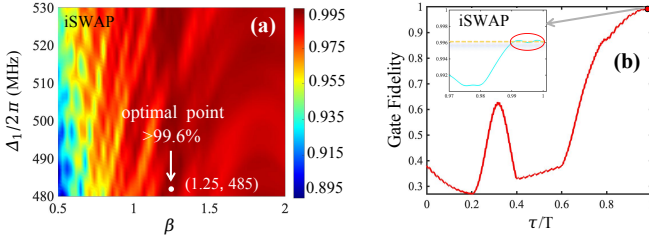


FIG. 10. (a)  $i\text{SWAP}^{\text{NNGQC}}$  gate in superconducting implementation as functions of tunable parameters  $\Delta$  and  $\beta$ , in which the comprehensive impacts of the neglected higher-order oscillating terms and the system decoherence are taken into account. The optimal point in white are the parameter region with the gate fidelity higher than 99.60%. (b) The dynamics of the gate fidelities for  $i\text{SWAP}^{\text{NNGQC}}$  gate under the optimal settings of  $\Delta, \beta$ .

320 MHz, while the qubit-parameter settings of transmon  $Q_2$  are determined to be anharmonicity  $\alpha = 2\pi \times 300$  MHz and decoherence rates  $\kappa_-^2 = \kappa_z^2 = 2\pi \times 2.3$  kHz [74–76]. In addition, the coupling strength between two transmons is set to  $g_{12} = 2\pi \times 8$  MHz.

From Eq. (29), it can be seen that the different selection of modulation parameters  $\{\beta, \nu\}$  is directly related to the impact of higher-order oscillating terms, including leakage error on the gate fidelity. Therefore, it is of necessity to further optimize  $\{\beta, \nu\}$  in order to enhance gate fidelity. As shown in Figs. 10 (a), we simulate the two-qubit gate fidelity as a function of  $\beta$  and  $\nu$ , where our  $i\text{SWAP}$  gate based on NNGQC can determine the parameter region (marked in red) with the gate fidelity higher than 99.60%. Such as, under the optimal parameter settings of  $\{\beta = 1.25, \Delta = 2\pi \times 485 \text{ MHz}\}$  our  $i\text{SWAP}$  gate can be as high as 99.61%, respectively, as shown in Figs. 10 (a) and 10 (b). Therefore, our NNGQC geometric two-qubit gates is able to possess strong robustness and high-fidelity performance in superconducting system.

## VI. CONCLUSION

In conclusion, we summarize the existing NNGQC framework and propose a new NNGQC scheme based on it, in which the generic non-adiabatic geometric gates can be constructed by noncyclic non-Abelian geometric phases. Compared with the conventional Rabi, NGQC and existing NNGQC, our new scheme not only breaks through the limitation of the cyclic condition and reduces the geometry gate time, but also shows great superiority under generalized robust control and crosstalk error. Moreover, we construct single-quantum bit gates and two-quantum  $i\text{SWAP}$  gates based on superconducting quantum circuits. Numerical simulations show that both our single and two logic quantum bit-geometry gates can exhibit high fidelity and strong robustness. Thus, our scheme provides a promising approach to fault-tolerant quantum computation for superconducting quantum circuits.

## ACKNOWLEDGMENTS

This work was supported by the National Natural Science Foundation of China (Grants No. 12305019, No. 12275090, and No. 12405009), Funding by Science and Technology Projects in Guangzhou (Grant No. 2024A04J4345), National College Students' Innovation Training Program (Grant No. 202410574037), and the Guangdong Provincial Quantum Science Strategic Initiative (Grant No. GDZX2203001).

## Appendix A: Parameter optimization based on class A noncyclic trajectory optimization

In this section, based on the optimization method in the main text, we can obtain the optimal solution under all trajectory optimization for  $S_{A2}^{1,2,3}$ . Specifically, under the condition for subcase  $(A_2): \xi(\tau) = \xi(0) \pm 2n\pi$  is satisfied, the evolution path first makes one or more one-turn loops in the latitudinal plane of the starting point and returns to it. Finally, it evolves along the longitudinal line to the end point. To be precise, the path is evolved from the start point  $\mathbf{P}_0(\chi_0, \xi_0)$  to the point  $\mathbf{P}_1(\chi_0, \xi_0 + 2n\pi)$  and finally reaching point  $\mathbf{P}_2(\chi_1, \xi_0 + 2n\pi)$  along the meridian.

A series of optimized paths can be planned by using this path fragment to extend and superimpose in different ways, we give two optimized paths as Fig. 2 (b) and account for the reasons. In the primitive path fragment  $S_{A2}^1$ , it is not difficult to observe that to construct the universal  $R_{x,y}(\pi)$  based on this path, the path parameters must satisfy  $\chi(\tau) - \chi(0) = \pi$ . This means that the start point and the end point must be located at the north and south poles, respectively. Obviously, this requirement implies that the single-loop evolution of the first segment cannot exist and degenerates into a mathematically meaningful set of points. At the same time, only the number of multi-loop wraparounds  $n$  is adjustable, resulting in a system with too few degrees of freedom. This limitation is not conducive to optimal design.

For this reason we introduced the  $S_{A2}^2$  path, compared to  $S_{A2}^1$  it has an extra segment of branching structure evolving along the meridian, which cleverly helps us realize the construction of the  $R_{x,y}(\pi)$  gate. Naturally, we wondered whether superposition of the  $S_{A2}^2$  path structure would not only expand its degrees of freedom, but also have unexpected results in its robustness. Based on this, we designed a path optimization of  $S_{A2}^3$ , a two-loop configuration. By optimizing the number of wraps  $n_1, n_2$  of the two latitude line evolutions, the fidelity of this scheme to construct a universal quantum gate can be greatly improved. It is worth noting that while repeated superposition of the structure can enhance robustness, too many composite structures will not only excessively prolong the evolution time but also introduce redundancy in parameter variables. This redundancy can ultimately lead to the failure of gate construction in experimental implementations. Therefore, combining all the influencing factors, the double-loop evolution of  $S_{A2}^3$  is the most ideal path optimization, and the numerical simulation will also verify our conclusion.



## Appendix B: Parameter optimization based on class B noncyclic path optimization

Meanwhile, the value of  $n$  cannot take zero for the following reason if  $n = 0$ , It's not hard to figure out  $\gamma_g = 0$  which destroys the pure geometric condition so rounded off, here for the convenience of the narrative, we tentatively consider  $n = 1$ , and it gives the final simplified gate operator which successfully achieves the construction of the standard rotating gates  $X$ ,  $Y$  and the Hadamard gates

Here it is especially important to account for the fact that the value of  $n$  in the  $R_z$  gate needs to be varied according to the negative integer value, by taking a negative value of it, we can ensure that the accumulated phase can be effectively controlled and adjusted in different loops or iterations to avoid unwanted phase shifts, and a negative value of  $n$  can help to simulate the phase change in such a non-closed path. Meanwhile in quantum systems, decoherence is an unavoidable phenomenon which leads to the loss of coherence of the quantum state. Negative values can also simulate the effect of decoherence on quantum gate operation, thus investigating how to achieve more robust quantum operation in real quantum systems. In fact, according to numerical simulations, we conclude that the value of  $n$  can be optimized as long as it is taken within the range around the saturation point, and is not mathematically different from that of the saturation point.

It is worth noting that, since in the second evolutionary segment  $\xi_2 - \xi_1 = (2n+1)\pi$ , therefore for different gates, we can optimize the parameter  $n$  on top of the original one to achieve the most desirable effect. In addition the fidelity of the gate increases logarithmically with  $n$ .

## Appendix C: Dynamical Rabi gate

The desire for better performance of geometric gates compared to conventional dynamical quantum gates is usually limited by the complex multilevel quantum bit interactions and the longer gate duration pulse times required. Therefore, we present the dynamic gates in detail here as a reference to highlight the higher gate fidelity and stronger robustness of our geometric gates. Assuming  $\hbar = 1$ , for a two-level system of  $\{|0\rangle = (1, 0)^T, |1\rangle = (0, 1)^T\}$  driven by an external microwave field. Under the rotating wave approximation, the system's Hamiltonian is given by

$$\mathcal{H}(t) = \frac{1}{2} \begin{pmatrix} -\Delta(t) & \Omega(t)e^{-i\phi(t)} \\ \Omega(t)e^{i\phi(t)} & \Delta(t) \end{pmatrix}, \quad (\text{C1})$$

where  $\Omega(t)$  and  $\phi(t)$  are the time-dependent driving amplitude and phase of the microwave field, respectively, and  $\Delta(t)$  represents the detuning relative to the frequency difference between the microwave field and the two-level system.

By setting the parameters  $\Delta = 0, \phi = \phi_d$ , the evolution operator for the dynamical evolution process is derived as

$$\begin{aligned} U_d(\theta_d, \phi_d) &= e^{-i \int_0^T \mathcal{H}(t) dt} \\ &= \begin{pmatrix} \cos \frac{\theta_d}{2} & -i \sin \frac{\theta_d}{2} e^{-i\phi_d} \\ -i \sin \frac{\theta_d}{2} e^{i\phi_d} & \cos \frac{\theta_d}{2} \end{pmatrix}, \end{aligned} \quad (\text{C2})$$

where  $\theta_d = \int_0^T \Omega(t) dt$ , while  $\phi_d$  is a constant in order to eliminate the geometrical phase. Based on the above, we can construct arbitrary rotating gates of the form:  $R_x^d(\theta_x) = U_d(\theta_x, 0)$ ,  $R_y^d(\theta_y) = U_d(\theta_y, \pi/2)$  and  $R_z^d(\theta_z) = U_d(\pi/2, \pi)U_d(\theta_z, -\pi/2)U_d(\pi/2, 0)$ . In addition, another set of single-bit universal quantum logic gates, Hadamard gates, phase gates, and  $\frac{\pi}{8}$  gates, can also be constructed by this principle:  $U_d(\pi, \pi)U_d(\pi/2, \pi/2)$ ,  $R_z^d(\pi/2)$  and  $R_z^d(\pi/4)$ .

## Appendix D: The Single-loop NGQG scheme

In this section, we describe in detail the construction of nonadiabatic geometric gates using the regular NGQG scheme. For resonance-driven two-energy quantum systems, the interacting Hamiltonian in the interaction picture is given by

$$\mathcal{H}(t) = \frac{1}{2} \begin{pmatrix} 0 & \Omega(t)e^{-i\phi_c} \\ \Omega(t)e^{i\phi_c} & 0 \end{pmatrix}, \quad (\text{D1})$$

where  $\Omega(t)$  and  $\phi_c$  denote the amplitude and phase of the driving field, respectively. In the conventional NGQG scheme, the total evolution time  $T$  is partitioned into three distinct segments to ensure geometric evolution. At the intermediate times  $T_1$  and  $T_2$ , the pulse area and relative phase  $\phi_c$  satisfy

$$\begin{cases} \int_0^{T_1} \Omega_c(t) dt = \theta_c, & \phi_c = \phi - \frac{\pi}{2}, & t \in [0, T_1], \\ \int_{T_1}^{T_2} \Omega_c(t) dt = \pi, & \phi_c = \phi + \gamma + \frac{\pi}{2}, & t \in [T_1, T_2], \\ \int_{T_2}^T \Omega_c(t) dt = \pi - \theta_c, & \phi_c = \phi - \frac{\pi}{2}, & t \in [T_2, T]. \end{cases} \quad (\text{D2})$$

Next, the evolution operator at the final time is

$$\begin{aligned} U_c(T) &= U_c(T, T_2)U_c(T_2, T_1)U_c(T_1, 0) \\ &= \cos \gamma + i \sin \gamma \begin{pmatrix} \cos \theta_c & \sin \theta_c e^{-i\phi} \\ \sin \theta_c e^{i\phi} & -\cos \theta_c \end{pmatrix} \\ &= e^{i\gamma \mathbf{n} \cdot \boldsymbol{\sigma}}, \end{aligned} \quad (\text{D3})$$

where  $\mathbf{n} = (\sin \theta_c \cos \phi, \sin \theta_c \sin \phi, \cos \theta_c)$  is a unit directional vector and  $\boldsymbol{\sigma} = (\sigma_x, \sigma_y, \sigma_z)$  is a Pauli vector. Therefore, any single-qubit geometric gate can be implemented by properly selecting the parameters  $\{\theta_c, \phi, \gamma\}$ . For example, the  $T$  gate and  $H^g$  gate correspond to the parameter sets  $\{0, 0, \pi/8\}$  and  $\{\pi/4, 0, \pi/2\}$ , respectively.

## Appendix E: Derivative removal by adiabatic gates (DRAG) correction

In practical physical realization, due to the weak anharmonicity of transmon, when our target microwave field is applied to the two lowest energy levels of transmon, the target driven on the quantum bit state will also stimulate the sequential transitions between the higher excited states in a dispersive manner at the same time, i.e., the sequential leaps between the higher excited states are induced at the same time, which leads to the leakage error. Here, considering the main leakage terms

of the quantum bit states we have chosen three energy levels for the calculation. At this stage, the Hamiltonian quantity describing a single quantum bit system can be written as

$$\mathcal{H}_1(t) = \frac{1}{2} \mathbf{B}(t) \cdot \mathbf{S} - \alpha_k |2\rangle\langle 2|, \quad (\text{E1})$$

where the operator vector  $\mathbf{S}$  is given by

$$\begin{aligned} S_x &= \sum_{k=0,1} \sqrt{k+1} (|k+1\rangle\langle k| + |k\rangle\langle k+1|), \\ S_y &= \sum_{k=0,1} \sqrt{k+1} (i|k+1\rangle\langle k| - i|k\rangle\langle k+1|), \\ S_z &= \sum_{k=0,1,2} (1-2k) |k\rangle\langle k|. \end{aligned}$$

And  $\alpha_k$  is the intrinsic anharmonicity of the target transmon,  $\mathbf{B}(t) = \mathbf{B}_0(t) + \mathbf{B}_d(t)$  is the vector of the total microwave field, containing the original microwave field and the additional DRAG-corrected microwave field term, i.e.,

$$\begin{aligned} \mathbf{B}_0(t) &= (B_x, B_y, B_z) \\ &= (\Omega(t) \cos(\phi_0 + \phi_1(t)), \Omega(t) \sin(\phi_0 + \phi_1(t)), -\Delta), \\ \mathbf{B}_d(t) &= (B_{d;x}, B_{d;y}, B_{d;z}) \\ &= -\frac{1}{2\alpha_k} (-\dot{B}_y + B_z B_x, \dot{B}_x + B_z B_y, 0), \end{aligned}$$

It is worth mentioning that through numerical simulations we find that for all physically realizable single-qubit geometric gates, their leakage error sensitivity due to leakage into the third energy level is less than 0.01%. This further indicates that the gate fidelity and robustness can be better improved by applying the DRAG technique correction in superconducting line systems.

- 
- [1] M. A. Nielsen and I. L. Chuang, *Quantum Computation and Quantum Information* (Cambridge University Press, 2000).
  - [2] M. V. Berry, Quantal phase factors accompanying adiabatic changes, *Proc. R. Soc. London A* **392**, 45 (1984).
  - [3] F. Wilczek and A. Zee, Appearance of gauge structure in simple dynamical systems, *Phys. Rev. Lett.* **52**, 2111 (1984).
  - [4] Y. Aharonov and J. Anandan, Phase change during a cyclic quantum evolution, *Phys. Rev. Lett.* **58**, 1593 (1987).
  - [5] J. Anandan, Non-adiabatic non-abelian geometric phase, *Phys. Lett. A* **133**, 171 (1988).
  - [6] Joseph Samuel and Rajendra Bhandari, General Setting for Berry's Phase, *Phys. Rev. Lett.* **60**, 2339 (1988).
  - [7] M. V. Berry, Quantal phase factors accompanying adiabatic changes, *Proc. R. Soc. London A* **392**, 45 (1984).
  - [8] F. Wilczek and A. Zee, Appearance of gauge structure in simple dynamical systems, *Phys. Rev. Lett.* **52**, 2111 (1984).
  - [9] Y. Aharonov and J. Anandan, Phase change during a cyclic quantum evolution, *Phys. Rev. Lett.* **58**, 1593 (1987).
  - [10] J. Samuel and R. Bhandari, General Setting for Berry's Phase, *Phys. Rev. Lett.* **60**, 2339 (1988).
  - [11] J. Anandan, Non-adiabatic non-abelian geometric phase, *Phys. Lett. A* **133**, 171 (1988).
  - [12] P. Zanardi and M. Rasetti, Holonomic quantum computation, *Phys. Lett. A* **264**, 94 (1999).
  - [13] J. Pachos, P. Zanardi, and M. Rasetti, Non-Abelian Berry connections for quantum computation, *Phys. Rev. A* **61**, 010305(R) (1999).
  - [14] J. A. Jones, V. Vedral, A. Ekert, and G. Castagnoli, Geometric quantum computation using nuclear magnetic resonance, *Nature* **403**, 869 (2000).
  - [15] L.-M. Duan, J. I. Cirac, and P. Zoller, Geometric manipulation of trapped ions for quantum computation, *Science* **292**, 1695 (2001).
  - [16] L. Faoro, J. Siewert, and R. Fazio, Non-Abelian Holonomies, Charge Pumping, and Quantum Computation with Josephson Junctions, *Phys. Rev. Lett.* **90**, 028301 (2003).
  - [17] H. R. Lewis and W. B. Riesenfeld, An exact quantum theory of the time-dependent harmonic oscillator and of a charged particle in a time-dependent electromagnetic field, *J. Math. Phys.* **10**, 1458 (1969).
  - [18] X. Chen, E. Torrontegui, and J. G. Muga, Lewis-Riesenfeld invariants and transitionless quantum driving, *Phys. Rev. A* **83**, 062116 (2011).
  - [19] A. Ruschhaupt, X. Chen, D. Alonso, and J. G. Muga, Optimally robust shortcuts to population inversion in two-level quantum systems, *New J. Phys.* **14**, 093040 (2012).
  - [20] Shi-Liang Zhu, Z. D. Wang, and Yong-Dong Zhang, Nonadiabatic noncyclic geometric phase of a spin- $\frac{1}{2}$  particle subject to an arbitrary magnetic field, *Phys. Rev. B* **61**, 1142 (2000).
  - [21] J. Samuel and R. Bhandari, General Setting for Berry's Phase, *Phys. Rev. Lett.* **60**, 2339 (1988).
  - [22] A. Friedenauer and E. Sjöqvist, Noncyclic geometric quantum computation, *Phys. Rev. A* **67**, 024303 (2003).
  - [23] F. De Zela, in *Theoretical Concepts of Quantum Mechanics*, edited by M. R. Pahlavani (InTech, London, 2012).
  - [24] W. Xiang-Bin and M. Keiji, Nonadiabatic conditional geometric phase shift with NMR, *Phys. Rev. Lett.* **87**, 097901 (2001).
  - [25] S.-L. Zhu and Z. D. Wang, Implementation of universal quantum gates based on nonadiabatic geometric phases, *Phys. Rev. Lett.* **89**, 097902 (2002).
  - [26] Axel Friedenauer and Erik Sjöqvist, Noncyclic geometric quantum computation, *Phys. Rev. A* **67**, 024303 (2003).
  - [27] E. Sjöqvist, D. M. Tong, L. M. Andersson, B. Hessmo, M. Johansson, and K. Singh, Non-adiabatic holonomic quantum computation, *New J. Phys.* **14**, 103035 (2012).
  - [28] G. F. Xu, J. Zhang, D. M. Tong, E. Sjöqvist, and L. C. Kwek, Nonadiabatic holonomic quantum computation in decoherence-free subspaces, *Phys. Rev. Lett.* **109**, 170501 (2012).
  - [29] J. Zhang, T. H. Kyaw, S. Filipp, L.-C. Kwek, E. Sjöqvist, and D. M. Tong, Geometric and holonomic quantum computation, *Phys. Rep.* **1027**, 1 (2023).
  - [30] G. F. Xu and G. L. Long, Protecting geometric gates by dynamical decoupling, *Phys. Rev. A* **90**, 022323 (2014).
  - [31] G. F. Xu, P. Z. Zhao, T. H. Xing, E. Sjöqvist, and D. M. Tong, Composite nonadiabatic holonomic quantum computation, *Phys. Rev. A* **95**, 032311 (2017).
  - [32] B. J. Liu, X. K. Song, Z. Y. Xue, X. Wang, and M. H. Yung, Plug-and-Play Approach to Nonadiabatic Geometric Quantum

- Gates, Phys. Rev. Lett. **123**, 100501 (2019).
- [33] T. Chen and Z.-Y. Xue, High-Fidelity and Robust Geometric Quantum Gates that Outperform Dynamical Ones, Phys. Rev. Appl. **14**, 064009 (2020).
- [34] Y. Dong, S.-C. Zhang, Y. Zheng, H.-B. Lin, L.-K. Shan, X.-D. Chen, W. Zhu, G.-Z. Wang, G.-C. Guo, and F.-W. Sun, Experimental implementation of universal holonomic quantum computation on solid-state spins with optimal control, Phys. Rev. Appl. **16**, 024060 (2021).
- [35] J. Preskill, Quantum computing in the NISQ era and beyond, Quantum **2**, 79 (2018).
- [36] W. Dong, F. Zhuang, S. E. Economou, and E. Barnes, Doubly Geometric Quantum Control, PRX Quantum **2**, 030333 (2021).
- [37] Tao Chen, Jia-Qi Hu, Cheng-xian Zhang, and Zheng-Yuan Xue, Universal robust geometric quantum control via geometric trajectory correction, Phys. Rev. Appl. **22**, 014060 (2024).
- [38] Tao Chen, Zheng-Yuan Xue and Z.D. Wang, Error-Tolerant Geometric Quantum Control for Logical Qubits with Minimal Resources, Phys. Rev. Appl. **18**, 014062 (2022).
- [39] Bao-Jie Liu, Shi-Lei Su, and Man-Hong Yung, Nonadiabatic noncyclic geometric quantum computation in Rydberg atoms, Phys. Rev. Research. **2**, 043130 (2020).
- [40] J. W. Zhang, L.-L. Yan, J. C. Li, G. Y. Ding, J. T. Bu, L. Chen, S.-L. Su, F. Zhou, and M. Feng, Single-Atom Verification of the Noise-Resilient and Fast Characteristics of Universal Nonadiabatic Noncyclic Geometric Quantum Gates, Phys. Rev. Lett. **127**, 030502 (2021).
- [41] Wen-Xin Xie, Chengxian Zhang, and Zheng-Yuan Xue, Universal Singlet-Triplet Qubits Implemented Near the Transverse Sweet Spot, Ann. Phys. (Berlin) 2021, 533, 2100054.
- [42] N. Eivarsen and E. Sjöqvist, Genuinely noncyclic geometric gates in two-pulse schemes, Phys. Rev. A **108**, 032612 (2023).
- [43] Y.-J. Hai, J. Li, J. Zeng, D. Yu, and X.-H. Deng, Universal robust quantum gates by geometric correspondence of noisy quantum evolution, arXiv:2210.14521.
- [44] P. M. Poggi, G. D. Chiara, S. Campbell, and A. Kiely, Universally Robust Quantum Control, Phys. Rev. Lett. **132**, 193801 (2024).
- [45] P. Mundada, G. Zhang, T. Hazard and A. Houck, Suppression of Qubit Crosstalk in a Tunable Coupling Superconducting Circuit, Phys. Rev. Applied **12**, 054023 (2019).
- [46] P. Zhao, D. Lan, P. Xu, G. Xue, M. Blank, X. Tan, H. Yu and Y. Yu, Suppression of Static ZZ Interaction in an All-Transmon Quantum Processor, Phys. Rev. Applied **16**, 024037 (2021).
- [47] Bradley K. Mitchell *et al.*, Hardware-Efficient Microwave-Activated Tunable Coupling between Superconducting Qubits, Phys. Rev. Lett. **127**, 200502 (2021).
- [48] A. Kandala *et al.*, Demonstration of a High-Fidelity CNOT Gate for Fixed-Frequency Transmons with Engineered ZZ Suppression, Phys. Rev. Lett. **127**, 130501 (2021).
- [49] J. Stehlik *et al.*, Tunable Coupling Architecture for Fixed-Frequency Transmon Superconducting Qubits, Phys. Rev. Lett. **127**, 080505 (2021).
- [50] Z. Ni *et al.*, Scalable Method for Eliminating Residual ZZ Interaction between Superconducting Qubits, Phys. Rev. Lett. **129**, 040502 (2022).
- [51] K.-X. Wei *et al.*, Hamiltonian Engineering with Multicolor Drives for Fast Entangling Gates and Quantum Crosstalk Cancellation, Phys. Rev. Lett. **129**, 060501 (2022).
- [52] S. Watanabe, Y. Tabuchi, K. Heya, S. Tamate and Y. Nakamura, ZZ-Interaction-Free Single-Qubit-Gate Optimization in Superconducting Qubits, Phys. Rev. A **109**, 012616 (2024).
- [53] R. Barends, J. Kelly, A. Megrant, A. Veitia, D. Sank, E. Jeffrey, T. C. White, J. Mutus, A. G. Fowler, and B. Campbell, *et al.*, Superconducting quantum circuits at the surface code threshold for fault tolerance, Nature (London) **508**, 500 (2014).
- [54] N. Didier, E. A. Sete, J. Combes, and M. P. da Silva, ac Flux Sweet Spots in Parametrically Modulated Superconducting Qubits, Phys. Rev. Appl. **12**, 054015 (2019).
- [55] S.-B. Zheng, C.-P. Yang, and F. Nori, Comparison of the sensitivity to systematic errors between nonadiabatic nonAbelian geometric gates and their dynamical counterparts, Phys. Rev. A **93**, 032313 (2016).
- [56] P.-Z. Zhao, X.-D. Cui, G.-F. Xu, E. Sjöqvist, and D. M. Tong, Rydberg-atom-based scheme of nonadiabatic geometric quantum computation, Phys. Rev. A **96**, 052316 (2017).
- [57] T. Chen and Z.-Y. Xue, Nonadiabatic geometric quantum computation with parametrically tunable coupling, Phys. Rev. Appl. **10**, 054051 (2018).
- [58] J. Clarke and F. K. Wilhelm, Superconducting quantum bits, Nature (London) **453**, 1031 (2008).
- [59] J. Q. You and F. Nori, Atomic physics and quantum optics using superconducting circuits, Nature (London) **474**, 589 (2011).
- [60] M. H. Devoret and R. J. Schoelkopf, Superconducting circuits for quantum information: An outlook, Science **339**, 1169 (2013).
- [61] P. Krantz, M. Kjaergaard, F. Yan, T. P. Orlando, S. Gustavsson, and W. D. Oliver, A Quantum Engineer's Guide to Superconducting Qubits, Appl. Phys. Rev. **6**, 021318 (2019).
- [62] M. Kjaergaard, M. E. Schwartz, J. Braumüller, P. Krantz, J. I.-Jan Wang, S. Gustavsson, and W. D. Oliver, Superconducting qubits: Current state of play, Annu. Rev. Condens. Matter Phys. **11**, 369 (2020).
- [63] He-Liang Huang, Dachao Wu, Daojin Fan, and Xiaobo Zhu, Superconducting quantum computing: A review, Sci. China Inf. Sci. **63**, 180501 (2020).
- [64] F. Motzoi, J. M. Gambetta, P. Reberntrost, and F. K. Wilhelm, Simple pulses for elimination of leakage in weakly nonlinear qubits, Phys. Rev. Lett. **103**, 110501 (2009).
- [65] J. F. Poyatos, J. I. Cirac, and P. Zoller, Complete Characterization of a Quantum Process: The Two-Bit Quantum Gate, Phys. Rev. Lett. **78**, 390 (1997).
- [66] Z.-q. Yin and F.-L. Li, Multiatom and resonant interaction scheme for quantum state transfer and logical gates between two remote cavities via an optical fiber, Phys. Rev. A **75**, 012324 (2007).
- [67] T. Wang, Z. Zhang, L. Xiang, Z. Jia, P. Duan, W. Cai, Z. Gong, Z. Zong, M. Wu, J. Wu, L. Sun, Y. Yin, and G. Guo, The experimental realization of high-fidelity "shortcut-to-adiabaticity" quantum gates in a superconducting Xmon qubit, New J. Phys. **20**, 065003 (2018).
- [68] S. Caldwell, N. Didier, C. A. Ryan, E. A. Sete, A. Hudson, P. Karalekas, R. Manenti, M. P. da Silva, R. Sinclair, E. Acala, *et al.*, Parametrically activated entangling gates using transmon qubits, Phys. Rev. Appl. **10**, 034050 (2018).
- [69] M. Reagor, C. B. Osborn, N. Tezak, A. Staley, G. Prawiroatmodjo, M. Scheer, N. Alidoust, E. A. Sete, N. Didier, M. P. da Silva, *et al.*, Demonstration of universal parametric entangling gates on a multi-qubit lattice, Sci. Adv. **4**, eaao3603 (2018).
- [70] K. Z. Li, P. Z. Zhao, and D. M. Tong, Approach to realizing nonadiabatic geometric gates with prescribed evolution paths, Phys. Rev. Res. **2**, 023295 (2020).
- [71] Z. Chen, J. Kelly, C. Quintana, R. Barends, B. Campbell, Y. Chen, B. Chiaro, A. Dunsworth, A. G. Fowler, E. Lucero, *et al.*, Measuring and suppressing quantum state leakage in a superconducting qubit, Phys. Rev. Lett. **116**, 020501 (2016).
- [72] F. Motzoi, J. M. Gambetta, P. Reberntrost, and F. K. Wilhelm, Simple Pulses for Elimination of Leakage in Weakly Nonlinear

- Qubits, Phys. Rev. Lett. **103**, 110501 (2009).
- [73] T. Wang, Z. Zhang, L. Xiang, Z. Jia, P. Duan, W. Cai, Z. Gong, Z. Zong, M. Wu, J. Wu, L. Sun, Y. Yin, and G. Guo, The experimental realization of high-fidelity ‘shortcut-to-adiabaticity’ quantum gates in a superconducting Xmon qubit, New J. Phys. **20**, 065003 (2018).
- [74] M. Kjaergaard, M. E. Schwartz, J. Braumüller, P. Krantz, J. I.-Jan Wang, S. Gustavsson, and W. D. Oliver, Superconducting qubits: Current state of play, Annu. Rev. Condens. Matter Phys. **11**, 369 (2020).
- [75] He-Liang Huang, Dachao Wu, Daojin Fan, and Xiaobo Zhu, Superconducting quantum computing: A review, Sci. China Inf. Sci. **63**, 180501 (2020).
- [76] C. Wang, X. Li, H. Xu, Z. Li, J. Wang, Z. Yang, Z. Mi, X. Liang, T. Su, C. Yang, *et al.*, Towards practical quantum computers: Transmon qubit with a lifetime approaching 0.5 ms, npj Quantum Inf. **8**, 1 (2022).
- [77] S. Caldwell, N. Didier, C. A. Ryan, E. A. Sete, A. Hudson, P. Karalekas, R. Manenti, M. P. da Silva, R. Sinclair, and E. Acala, *et al.*, Parametrically Activated Entangling Gates Using Transmon Qubits, Phys. Rev. Appl. **10**, 034050 (2018).
- [78] M. Reagor, C. B. Osborn, N. Tezak, A. Staley, G. Prawiroatmodjo, M. Scheer, N. Alidoust, E. A. Sete, N. Didier, M. P. da Silva, *et al.*, Demonstration of universal parametric entangling gates on a multi-qubit lattice, Sci. Adv. **4**, eaao3603 (2018).
- [79] J. Chu, D. Li, X. Yang, S. Song, Z. Han, Z. Yang, Y. Dong, W. Zheng, Z. Wang, X. Yu, D. Lan, X. Tan, and Y. Yu, Realization of Superadiabatic Two-Qubit Gates Using Parametric Modulation in Superconducting Circuits, Phys. Rev. Appl. **13**, 064012 (2020).